Water and ions binding to extracellular matrix drives stress relaxation, aiding MRI detection of swelling-associated pathology

Check for updates

Matthias R. Kollert [1,2], Martin Krämer [3,4], Nicholas M. Brisson [1], Victoria Schemenz[5], Serafeim Tsitsilonis[1,6], Taimoor H. Qazi [7], Peter Fratzl [8], Viola Vogel [2], Jürgen R. Reichenbach [4] & Georg N. Duda [1,6] ✉

Swelling-associated changes in extracellular matrix (ECM) occur in many pathological conditions involving inflammation or oedema. Here we show that alterations in the proportion of loosely bound water in ECM correlate with changes in ECM elasticity and stress relaxation, owing to the strength of water binding to ECM being primarily governed by osmolality and the electrostatic properties of proteoglycans. By using mechanical testing and small-angle X-ray scattering, as well as magnetic resonance imaging (MRI) to detect changes in loosely bound water, we observed that enhanced water binding manifests as greater resistance to compression (mechanical or osmotic), resulting from increased electrostatic repulsion between negatively charged proteoglycans rather than axial contraction in collagen fibrils. This indicates that electrostatic contributions of proteoglycans regulate elasticity and stress relaxation independently of hydration. Our ex vivo experiments in osmotically modulated tendon elucidate physical causes of MRI signal alterations, in agreement with pilot in vivo MRI of inflammatory Achilles tendinopathy. We suggest that the strength of water binding to ECM regulates cellular niches and can be exploited to enhance MRI-informed diagnostics of swelling-associated tissue pathology.

The extracellular matrix (ECM) of musculoskeletal tissues plays crucial roles in physiology by providing stability to organs, serving as scaffold to cells, and enabling force transmission over short and long distances. Beyond a diversity of biochemical functions, the ECM defines physical cues sensed by cells and thus guides their behaviour in vivo. Water is a main component of intra- and extracellular microenvironments in living tissues (for example, 62 wt% in tendon[1]). Water provides diffusivity, hydration and swelling pressure owing to hygroscopic ECM properties[2].

ECM hygroscopic properties are predominantly defined by proteoglycans (PGs), which play a key role in regulating water content and water binding owing to the electrostatic effects of their negative charges (for example, sulfate and carboxyl groups)[2,3]. These polyelectrolytes have a high capacity to retain ions and water[3], capable of generating osmotic pressures on the order of 400 kPa, which falls within the range of maximum tension in muscles[4–6]. However, injury, inflammation and diseases can affect these ECM properties and thereby their function as

[1]Julius Wolff Institute and BIH Center for Regenerative Therapies, Berlin Institute of Health at Charité - Universitätsmedizin Berlin, Berlin, Germany. [2]Laboratory of Applied Mechanobiology, Department of Health Sciences and Technology, ETH Zurich, Zurich, Switzerland. [3]Institute of Diagnostic and Interventional Radiology, Jena University Hospital, Friedrich Schiller University Jena, Jena, Germany. [4]Medical Physics Group, Institute of Diagnostic and Interventional Radiology, Jena University Hospital, Friedrich Schiller University Jena, Jena, Germany. [5]Department of Operative, Preventive and Pediatric Dentistry, Charité - Universitätsmedizin Berlin, Berlin, Germany. [6]Center for Musculoskeletal Surgery, Charité—Universitätsmedizin Berlin, Berlin, Germany. [7]Weldon School of Biomedical Engineering, Purdue University, West Lafayette, IN, USA. [8]Department of Biomaterials, Max Planck Institute of Colloids and Interfaces, Potsdam, Germany. ✉e-mail: georg.duda@charite.de
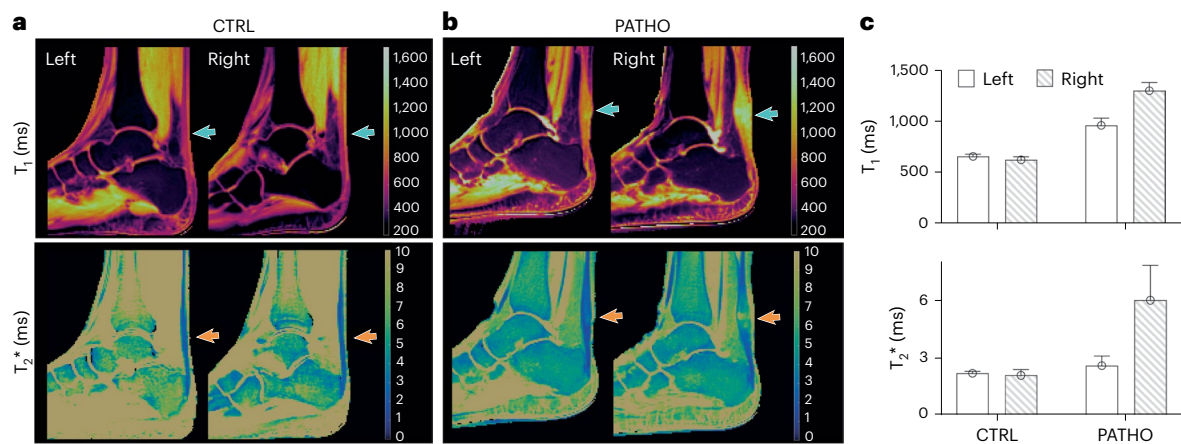
Fig. 1 | In vivo MRI scans of Achilles tendons showing swelling-related alterations in T_1 and T_2^*. a,b, Case study of clinical MRI scans of asymptomatic control subject (CTRL) (**a**) versus patient (PATHO) (**b**) with a diagnosed mechanopathology (mid-portion Achilles tendinopathy) in their right foot ($n = 1$). Representative parameter maps of sagittal planes show T_1 (top row) and T_2^* (bottom row). Arrows point to the mid-portion of the Achilles tendons. **c**, Quantification of T_1 (top) and T_2^* (bottom) in the mid-portions of the left and right Achilles tendons. Bar plots show mean ± s.d. of a region of interest from $n = 1$ Achilles tendon mid-portions.

cell niches. Various pathologies are characterized by osmotic imbalances and related acute or chronic dysregulations of the involved ECM (for example, deranged PG content or modified water binding), which are characteristic of inflammation[7], swelling[8], oedema[8,9], some forms of cancer[10–12] and scarring[13,14]. Within physiological limits, osmotic alterations regulate many essential processes in organs. For instance, osmotic pressure can strongly affect soft tissue tension and cell behaviour[15–18], or regulate swelling after injury or infection[8,19]. So far, however, it remains unknown how osmotic dysregulation affects specifically the stress-relaxation material properties of the ECM. Recently, elastic and stress-relaxation properties of the ECM have been identified as being crucial for determining cell phenotype and fate, thereby guiding cell behaviour (for example, spreading, migration and differentiation[20–22]). Changes in these elastic and stress-relaxation properties may indicate pathological tissue alterations (for example, scarring and tumour progression[12,22]).

Tendons mainly consist of water, collagen fibres and PGs, which are among the most abundant ECM components in the body. Thus, characterization of tendon ECM as a model may lead to findings also transferable to other tissue types[23]. To study the effects of ECM water-binding properties and (de)hydration, an ex vivo ECM model, together with an experimental set-up that allowed to deliberately modulate the osmotic environment of a probe, was developed and used to characterize the mechanical, structural and magnetic resonance properties of soft tissues. The ex vivo ECM model was based on fresh, excised ovine Achilles tendon tissue, leveraging its organized structure to minimize potential confounding effects of diverse fibre directions on measurements. The ECM samples were exposed to defined osmotic environments using as osmolytes either ions to modulate water-binding strength (and thus electrostatic effects) or macromolecules to modulate the overall water content (that is, by dehydration). Water molecules are bound at different levels of strength in hydration layers around macromolecules in the ECM[24]. To detect changes in swelling and water binding non-invasively, we used quantitative magnetic resonance imaging (MRI) mapping because the presence and mobility of water molecules or protons influence magnetic resonance signal relaxation[25,26]. MRI relaxation parameters—such as T_1 and T_2^*—were proposed to be used as biomarkers for tissue hydration[27–29] and have previously been related to water binding in hydration layers around macromolecules in living tissues[25]. To detect alterations in the proportion of more loosely bound water in the ECM, we used T_2^* (ref. 30). To quantify elastic and stress-relaxation properties, we used

uniaxial compression testing[21]. For multi-scale structural analysis, we performed histological staining, small-angle X-ray scattering (SAXS) and high-resolution MRI.

We hypothesized that the ionic concentration of a local osmotic environment regulates ECM elastic and stress-relaxation properties by tuning water-binding properties, and indeed we found this confirmed in mechanical, structural and MRI-characterization experiments. We aimed to reflect traits of swelling-related pathologies with the developed ex vivo ECM model and experimental set-up, which we confirmed with clinical in vivo MRI scans in a human case study of a mechanopathology (Achilles tendinopathy), thereby underscoring the clinical implications of our findings. The observed ECM alterations were distinct from the effects of ECM dehydration, which we substantiated by using macromolecules as osmolytes and detailed structure analysis by SAXS. MRI relaxation parameters (T_1 and T_2^*) allowed to distinguish between distinct swelling-related ECM alterations and associated changes in biophysical properties (swelling, elastic modulus and stress relaxation), as demonstrated by independent correlations, illustrating the potential of our results to eventually advance non-invasive diagnostics.

Results

In vivo MRI scans of swelling-related pathological ECM alterations
We used ultra-short echo-time (UTE) MRI sequences for detecting swelling-related pathological ECM alterations. We started by mapping T_1 and T_2^* relaxation within a clinical case study of in vivo MRI scans. MRI scans were performed on one asymptomatic control subject (CTRL) and one patient diagnosed with mid-portion Achilles tendinopathy in their right foot (PATHO), a mechanopathology caused by aberrant loading (Supplementary Fig. 1). For CTRL, T_1 and T_2^* maps in the sagittal plane showed similar values for tendon mid-portions of left and right feet (Fig. 1a). By contrast, for PATHO, T_1 and T_2^* in the sagittal plane were higher in the right foot with tendinopathy than in the left foot (warmer colour, Fig. 1b). Subsequently, T_1 and T_2^* were quantified in tendon mid-portion volumes. T_1 was higher for PATHO (left, 971 ms; right, 1,309 ms) compared with CTRL (left, 664 ms; right, 630 ms) (Fig. 1c, top). T_2^* was higher particularly in the patient's affected foot (left, 2.6 ms; right, 6.0 ms) compared with CTRL (left, 2.2 ms; right, 2.1 ms) (Fig. 1c, bottom). These T_1 and T_2^* values were in line with observations from parameter maps in the sagittal plane (Fig. 1b). The observation of higher T_1 and T_2^* values in PATHO compared with CTRL was in line with previous studies (Supplementary Fig. 2, Supplementary
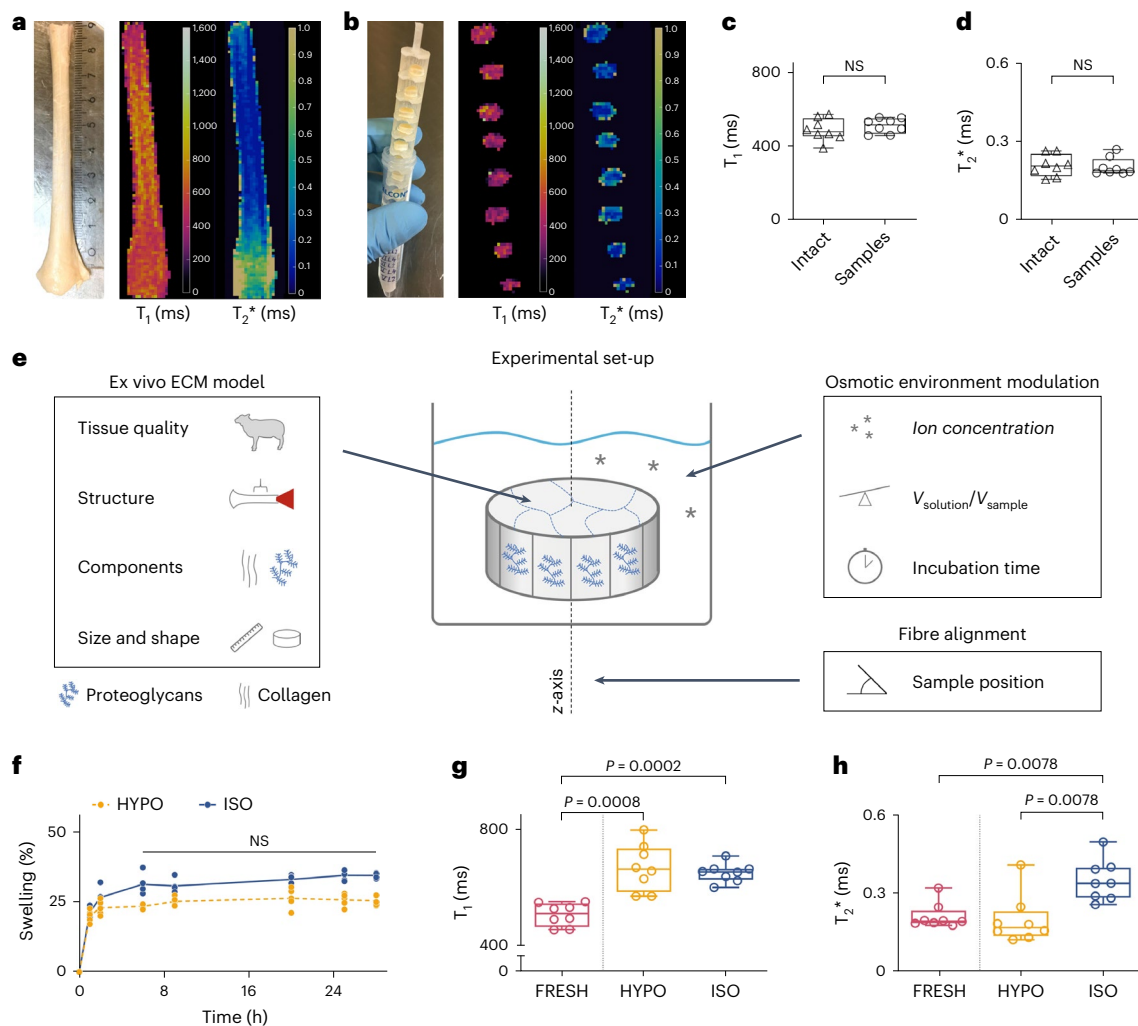
Fig. 2 | Physical ex vivo characterization of dissected Achilles tendon tissue showing that MRI T_1 and T_2^* detect osmotic environment-induced ECM alterations related to water binding. a, Left: representative image of an Achilles tendon; right: representative T_1 and T_2^* maps of an intact tendon. **b**, Left: customized 3D-printed sample mounting device that enabled aligned ECM sample positioning and controlled exposure to different osmotic environments for multiple samples; right: representative T_1 and T_2^* maps of ECM samples in FRESH condition. **c,d**, FRESH condition T_1 values (**c**) and T_2^* values (**d**) in mid-portions of intact tendons versus dissected ECM samples revealed no significant differences. *P* values were calculated using two-tailed *t*-tests for *n* = 8 biological samples. Significance threshold: *P* < 0.05; NS, not significant. **e**, The developed ex vivo ECM model and experimental set-up that enabled the tuning of ECM properties by modulating the osmotic environment (for example, by ion concentration). Other parameters of the ECM model (ex vivo ECM model),

incubation condition (osmotic environment modulation) and sample positioning (fibre alignment) were kept consistent to enable reproducible MRI and mechanical characterization. **f**, Gravimetric swelling recorded over time of ECM samples exposed to HYPO and ISO solutions showed that approximate equilibrium was reached after 6 h of incubation. *P* values were determined using a two-way analysis of variance (ANOVA) with Tukey's multiple comparisons for *n* = 5 samples from one tendon. **g,h**, T_1 values (**g**) and T_2^* values (**h**) of ECM samples in FRESH condition and after 24 h of swelling in HYPO or ISO solution showed differences in water uptake characteristics depending on the osmotic environment. *P* values were calculated for *n* = 8 biological samples in **g** using two-tailed *t*-tests and in **h** using two-tailed Wilcoxon signed-rank tests. Box plot information: box limits show 25th and 75th percentiles, box middle lines show medians, and whiskers show minimum and maximum values.

Note 1). Quantification of tendon thickness showed higher values in the mid-portion in the patient's affected foot, suggesting tissue swelling (Extended Data Fig. 1). Notably, for the patient, T_1 values were also higher in the contralateral unaffected foot of the patient, possibly owing to compensatory gait leading to an onset of pathological ECM alterations. To compare tendon MRI scans performed with UTE sequences (which enable mapping of T_1 and T_2^* parameters) with standard clinical sequences, one additional patient with diagnosed mid-portion Achilles tendinopathy was scanned (Extended Data Fig. 2). A comparison of the MR images obtained using these different imaging sequences shows that the UTE-based quantitative T_1 and T_2^* maps provide an additional level of insight and detail into tissue properties by T_1 and T_2^* mapping.

Mid-portion of Achilles tendon as an ex vivo ECM model
We validated fresh ex vivo mid-portions of ovine Achilles tendons as an ECM model by comparing the MRI relaxation parameters between intact tendon and dissected ECM samples first. Figure 2a shows fresh intact tendon (left) and the associated T_1 (middle) and T_2^* (right) maps of a representative tendon cross-section. T_2^* increased from the mid-tendon to the enthesis (bottom). In the mid-portion of the tendon, T_1 and T_2^* remained constant. Subsequently, ECM samples were dissected from tendon mid-portions and imaged anew in freshly dissected condition (FRESH) in a three-dimensional (3D)-printed mounting device (Fig. 2b, left). The observed T_1 and T_2^* in parameter maps (Fig. 2b, middle and right) were similar to those observed for intact tendon mid-portions (Fig. 2a). Quantification of these values in intact tendon
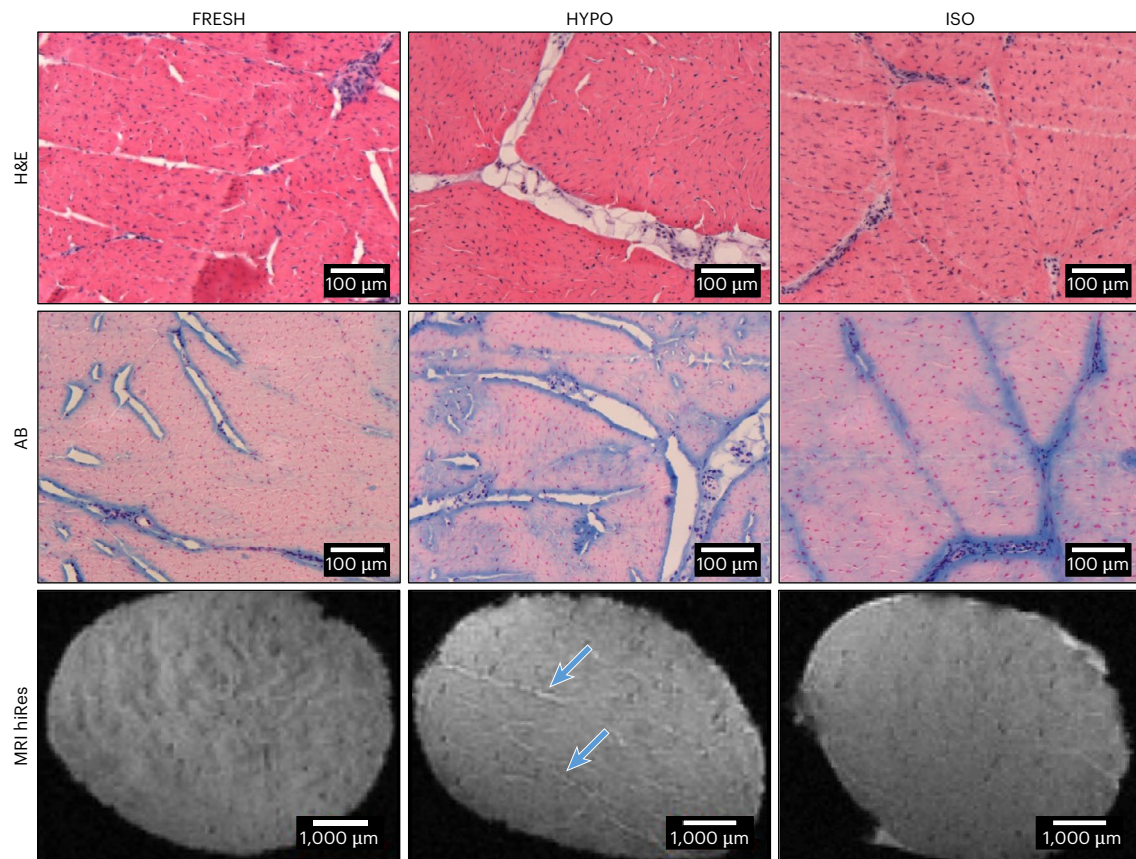
Fig. 3 | ECM stains of dissected mid-plane Achilles tendon cross-sections showing structural alterations owing to swelling and osmotic environment changes. Representative images of ECM cross-sections of FRESH (left column), HYPO (middle column) and ISO (right column) conditions are shown. Histological stainings are presented for (top row) H&E, showing collagen ECM in pink and cell nuclei as blue dots, and (middle row) AB, showing PGs in blue and cell nuclei as red. High-resolution MR images (MRI hiRes, bottom row) were acquired using a 9.4 T preclinical scanner, showing white lines with increased signal intensities (blue arrows), indicating increased amounts of accumulated water in the ECM. In AB images, increased blue staining in and along the IF matrix confirms high PG density in the IF matrix. Expanded IF regions in HYPO compared with FRESH and ISO conditions were visible in H&E and AB stainings and suggest increased PG water binding, which is supported by the white lines in the MRI hiRes images that are similar in width to the IF regions in the H&E and AB stainings.

mid-portion and ECM sample volumes confirmed no significant difference with T_1 values of 485 ms versus 506 ms (Fig. 2c) and T_2^* values of 0.208 ms versus 0.212 ms (Fig. 2d). The developed experimental set-up enables consistent ECM model properties, modulation of the osmotic environment and alignment of ECM fibre orientation (Fig. 2e). The latter was required especially for reproducible MRI characterization. The set-up allows to combine ECM characterization for structure, mechanics, osmotic environments and MRI relaxation parameters to investigate the interplay between osmolality, swelling and water binding, and their effects on elastic and stress-relaxation properties.

T_1 and T_2^* mapping of freshly dissected tissue samples reveals osmolality-tuned tight water binding to the ECM

To investigate how osmotic environments affected ECM hydration and water binding, T_1 and T_2^* mapping was performed in vitro. Using the described experimental set-up, we tested the incubation time required to reach swelling equilibrium for freshly dissected ECM samples exposed to hypo-osmolar (HYPO) or iso-osmolar (ISO) solutions, showing that equilibrium was reached after 6 h (Fig. 2f). To ensure equilibrium swelling and feasibility of measurement logistics, incubation time was set to 24 h for all subsequent experiments (Supplementary Fig. 3). ECM samples swelled in both HYPO and ISO after 24 h (Extended Data Fig. 3). T_1 increased for HYPO (669 ms) and ISO (651 ms) compared with FRESH (506 ms) (Fig. 2g). T_2^* remained unchanged in HYPO (0.197 ms), but it increased in ISO (0.349 ms), compared with FRESH (0.212 ms) (Fig. 2h), showing different characteristics than T_1. However,

results for T_1 and T_2^* suggest that the water uptake in HYPO was more strongly bound within the ECM, presumably by PGs, whereas in ISO an increased proportion of more loosely bound water was present. This increased amount of more strongly bound water in HYPO compared with ISO suggests enhanced electrostatic effects in the ECM in HYPO. By contrast, increasing the environmental ion concentration by 27% and 100% relative to ISO condition did not change T_1, T_2^* or swelling (Extended Data Fig. 4a–c). This suggests that in ISO, the proportion of more loosely bound water was already at a high level and that the decreasing effect of higher environmental ion concentrations on water-binding strength had saturated. This observation supported the experimental design that focused on comparing HYPO and ISO conditions to yield low or high proportions of more loosely bound water in the ECM, respectively. The pronounced difference in ECM water binding between the conditions facilitated investigating its role for ECM structural and mechanical properties. The increases in T_1, T_2^* and swelling from FRESH to ISO showed similar characteristics to those observed in the in vivo scans of CTRL versus PATHO (Fig. 1a–c and Extended Data Fig. 1), suggesting that our ex vivo ECM model with osmotic environment modulation has the potential to reflect traits of pathological ECM alterations.

ECM structure is altered by osmotic modulation

To better understand causes of the observed changes in MRI relaxation parameters that indicated decreased proportions of more loosely bound water in HYPO condition, we analysed the microscopic structure
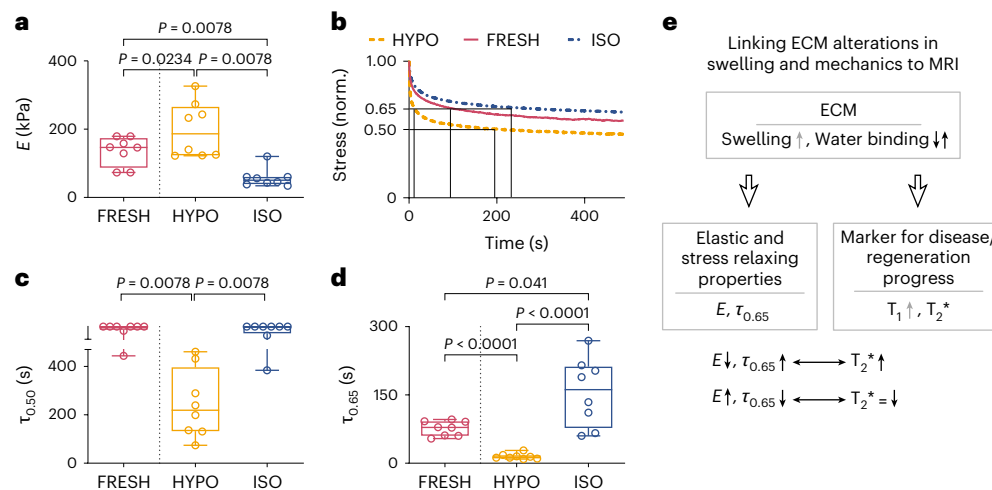
Fig. 4 | The ion concentration of the osmotic environment regulates the ECM elastic and stress-relaxation properties of ex vivo Achilles tendon. Mechanical characterization of ECM samples was performed for FRESH, HYPO and ISO conditions. **a**, Elastic modulus E. P values were calculated using two-tailed Wilcoxon signed-rank tests for $n = 8$ biological samples. **b**, The stress-relaxation behaviour is described by the relaxation of the applied peak stress at a maximum strain over time, which is shown with representative stress-relaxation curves of stress normalized (norm.) by the initial stress. **c**, The time until 50% of the peak stress was released was quantified by $\tau_{0.50}$. P values were determined using two-tailed Wilcoxon signed-rank tests for $n = 8$ biological samples. **d**, The time until 35% of the peak stress was released was quantified by $\tau_{0.65}$. P values were calculated using two-tailed t-tests for $n = 8$ biological samples. Box plot information: box limits show 25th and 75th percentiles, box middle lines show medians, and whiskers show minimum and maximum values. **e**, Schematic illustrating how alterations in ECM swelling and water-binding strength relate to changes in mechanics (E, $\tau_{0.65}$) and MRI relaxation parameters (T_1, T_2^*), and associated relationships between ECM mechanical properties and MRI parameters.

in representative ECM cross-sections using histological stainings. Haematoxylin and eosin (H&E) stained collagen ECM in pink and cell nuclei in blue, and Alcian Blue (AB) stained negatively charged PGs in blue and ECM in light pink. H&E images showed light lines at tendon fascicle edges[31] and were clearly expanded in HYPO, with parts of the delicate interfascicular (IF) matrix having been flushed away during the staining process, leaving unstained spaces (Fig. 3, top). AB images showed increased PG density in and around the IF connective tissue, as expected, compared with the collagen-rich fascicles (Fig. 3, middle). The expanded PG-rich IF regions in HYPO, visible in H&E and AB images, suggested that in the less-restricted IF matrix, enhanced electrostatic repulsion caused the expansion and led to a greater accumulation of water compared with FRESH and ISO conditions.

To verify this histological finding, we used high-resolution MRI with a 9.4 T preclinical scanner to obtain non-invasive insight into the tissue structure (Fig. 3, bottom). Light voxels depicted high signal intensities associated with increased amounts of accumulated water. MRI scans showed white lines with high signal intensity for tissue in HYPO, in contrast to FRESH and ISO. The white lines in HYPO corresponded to a width of 70–140 µm and thus were of similar magnitude as the approximately 100 µm wide expanded IF regions visible in H&E and AB stainings. Taken together, the histological stainings and high-resolution MR images indicate that ECM alterations in HYPO condition are due to increased water binding and electrostatic effects by PGs.

ECM mechanics are regulated by osmolality-tuned water binding properties

To understand the effects of the osmolality-tuned water binding and swelling on elastic and stress-relaxation properties of dissected Achilles tendon, bulk mechanical properties of ECM samples were quantified. The elastic modulus E of ECM samples increased from FRESH (136 kPa) to HYPO (198 kPa) and decreased in ISO (57 kPa) (Fig. 4a). These changes suggested that decreased proportions of more loosely bound water in HYPO (Fig. 2f and h) were associated with higher compressive resistance of ECM samples. By contrast, with increased proportions of more loosely bound water in ISO (Fig. 2f and h), we observed decreased E.

The decrease in E for ISO swelling relative to FRESH condition aligns with recent findings for spine-disk samples[32].

To further analyse the ECM stress-relaxation behaviour, the dissipation of applied stress over time was recorded. Representative stress-relaxation curves for HYPO and ISO conditions compared with FRESH condition (resembling physiological tissue more closely) showed faster and slower decays, respectively, reflecting the influence of the different osmotic environments on the ECM stress-relaxation behaviour (Fig. 4b). Subsequently, stress-relaxation properties were quantified using stress-relaxation half time $\tau_{0.50}$, a widely applied parameter in biomaterial and tissue engineering[21]. We found a strong decline in $\tau_{0.50}$ from FRESH (>500 s) to HYPO (245 s), while values remained at similar levels in ISO (>500 s) condition (Fig. 4c). Further insight into ECM stress-relaxation behaviour was achieved by using $\tau_{0.65}$, reflecting the early dissipation of applied stress. $\tau_{0.65}$ decreased from FRESH (76 s) to HYPO (15 s) and, conversely, increased in ISO (156 s) (Fig. 4d). By contrast, when the environmental ion concentration was increased by 27% and 100% relative to ISO condition, ECM mechanics did not change (Extended Data Fig. 4d–f). In these two conditions of increased ion concentrations, swelling and the proportion of more loosely bound water were at levels comparable to ISO (Extended Data Fig. 4a–c). Together with the absence of clear changes in ECM mechanics, these observations support the notion that between HYPO and ISO conditions, the substantial differences in ECM mechanics were caused by changes in electrostatic effects, as indicated by changes in water binding. These results demonstrate that ECM mechanics were tuned by environmental ion concentration when the proportion of more loosely bound water in the ECM was altered, suggesting that altered electrostatic properties caused the changes in mechanics. HYPO caused higher elastic moduli, which is in line with previous findings[3], as well as faster stress relaxation compared with ISO.

To verify that observed changes in mechanics were due to ECM components (for example, PGs) rather than to potential influences of cells in the tissue (for example, contractile forces), two additional experiments were performed. Alternating exposure of ECM samples to HYPO and ISO solutions showed the reversibility of the mechanical
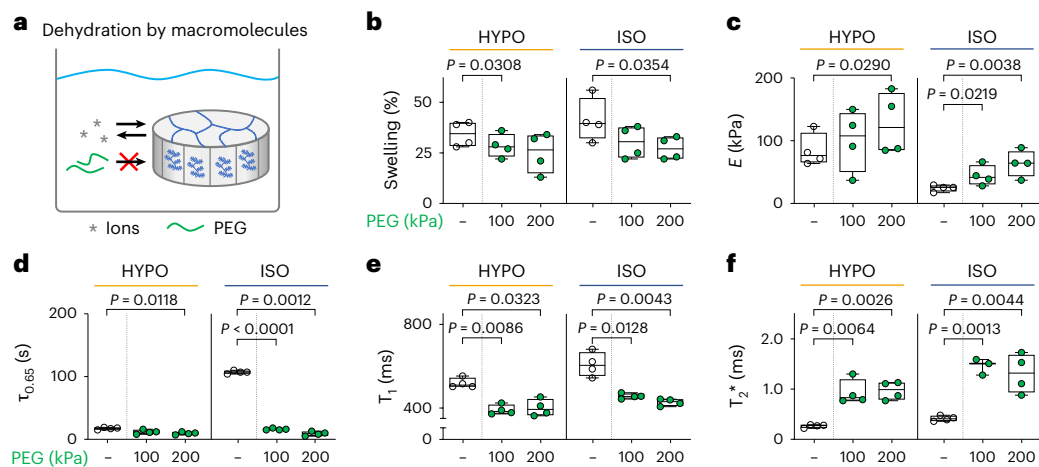
Fig. 5 | Application of osmotic pressure reveals that dehydration induces distinct ECM alterations compared with modulating osmolality through ion concentration. a, Illustration of the differences between two types of osmolyte: ions can diffuse into ECM samples, while high-molecular-weight macromolecules such as PEG cannot. Thus, the addition of PEG applies osmotic pressure to an ECM sample that leads to its dehydration (that is, decreased swelling). **b**–**f**, ECM samples were characterized by swelling (**b**), elastic modulus E (**c**), stress-relaxation time $\tau_{0.65}$ (**d**), T_1 values (**e**) and T_2^* values (**f**). P values were calculated using two-tailed t-tests for $n = 4$ biological samples, except in **f**, which used $n = 3$ biological samples for the comparison involving the ISO + 100 condition. The analyses compared conditions with added PEG to their respective reference condition (that is, either HYPO or ISO). Box plot information: box limits show 25th and 75th percentiles, box middle lines show medians, and whiskers show minimum and maximum values. Osmotic pressures of 100 kPa and 200 kPa were applied by PEG (5,000 molecular weight) concentrations of 8 wt% and 11 wt%, respectively.

changes (Extended Data Fig. 5). Further, ECM samples initially used for MRI characterization (Fig. 2) were subsequently subjected to mechanical characterization 5 days after excision, with storage and incubation at 4 °C between measurements. Mechanical characterization showed mechanical properties in HYPO and ISO similar to those in ECM samples already analysed 2 days after excision (Extended Data Fig. 6). Both experiments suggest that ECM components caused the observed changes in elastic and stress-relaxation properties.

Alterations in ECM swelling and mechanics can be distinguished by combined T_1 and T_2^* mapping

Next, the aforementioned measurement datasets for FRESH, HYPO and ISO conditions were analysed using Pearson's r to assess independent correlations, thereby elucidating the potential to non-invasively detect alterations in ECM swelling and mechanics based on changes in MRI and T_2^*. For T_1, a positive correlation was found with swelling ($r = 0.64$, $P = 0.001$), but not with mechanical parameters E ($r = 0.10$, NS) or $\tau_{0.65}$ ($r = -0.07$, NS). For T_2^*, correlations were based on the observed changes in each parameter between FRESH, HYPO and ISO conditions, denoted by Δ. ΔT_2^* did not correlate with Δswelling ($r = 0.30$, NS), but instead negatively correlated with ΔE ($r = -0.74$, $P < 0.0001$) and positively correlated with $\Delta\tau_{0.65}$ ($r = 0.76$, $P < 0.0001$), contrasting the correlations of T_1. Taken together, these results demonstrate the potential of combining T_1 and T_2^* to distinguish between alterations in ECM swelling and water-binding properties (for example, in pathological ECM alterations) and related changes in ECM mechanical properties (E, $\tau_{0.65}$), as shown schematically in Fig. 4e.

Tissue dehydration leads to different ECM mechanics and different T_2^* signal

Hyper-osmolar conditions can occur in physiology and pathology, with one scenario being increased osmotic pressure with effects similar to tissue dehydration (for example, solid-tumour environments[12,33]). To better understand how altered molecular crowding affects ECM properties compared with altered water-binding strength, as shown above, ECM samples were subjected to different concentrations of 5 kDa polyethylene glycol (PEG) macromolecules. These uncharged macromolecules are expected to exert osmotic

pressure on ECM samples by being unable to diffuse into ECM samples, in contrast to ions in the solution (Fig. 5a). PEG was added to HYPO and ISO solutions in concentrations to yield osmotic pressures of 100 kPa and 200 kPa, magnitudes previously shown to be physiologically relevant (for example, regulating stem cell fate[17,18]). It should be noted that the ion concentration of the ISO solution was assumed to have an equivalent osmotic pressure of 744 kPa. With PEG-induced osmotic pressures, samples showed signs of dehydration with swelling decreased at 100 kPa in HYPO (17%) and at 200 kPa in ISO (34%) (Fig. 5b). Osmotic pressure increased E at 200 kPa in HYPO (50%) and at 100 kPa and 200 kPa in ISO (81% and 160%) (Fig. 5c), with the change in E in ISO in agreement with previous studies on tissue dehydration[15,32]. $\tau_{0.65}$ decreased for 200 kPa in HYPO (45%) and for 100 kPa and 200 kPa in ISO (85% and 92%) (Fig. 5d). T_1 decreased at osmotic pressures of 100 kPa and 200 kPa in HYPO (25% and 23%) and in ISO (25% and 30%) (Fig. 5e), which was in line with its aforementioned correlation with swelling. T_2^* increased substantially with applied osmotic pressure of 100 kPa and 200 kPa in both HYPO (252% and 266%) and ISO (252% and 216%) (Fig. 5f). These increases in T_2^* clearly exceeded the 65% increase observed when comparing FRESH with ISO (Fig. 2h) that resulted in strongly decreased E and increased $\tau_{0.65}$ (Fig. 4). In HYPO, swelling and T_1 appeared to decrease less at 200 kPa osmotic pressure than in ISO. This observation was in line with the decreased proportions of loosely bound water in HYPO, relating to higher swelling pressure within the ECM, and thus to enhanced resistance to the applied mechanical (as seen with E) or osmotic (as seen with swelling) compression. The observation that osmotic pressure increased E and decreased $\tau_{0.65}$ in HYPO and ISO suggests that water-binding properties regulate elastic and stress-relaxation properties independently from (de)hydration, thus involving a different mode of osmolality–ECM interaction. The particularly large increase in T_2^* in PEG conditions suggests that combined T_1 and T_2^* mapping could have the potential to distinguish ECM alterations caused by applied osmotic pressure from alterations related to swelling and altered water binding. The greater change in T_2^* could be caused by effects of dehydration, previously shown capable of causing collagen fibre contraction and, thus, tissue contraction[15]. These findings suggest that osmotic pressure (or mechanical loading) induced tissue contraction, altered
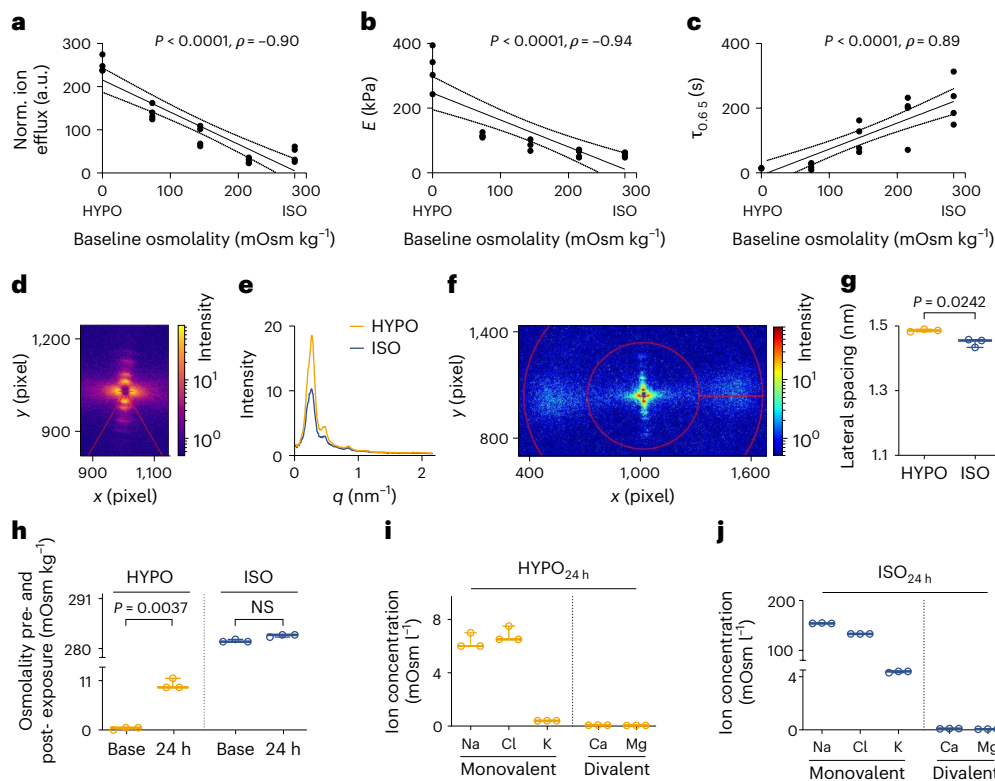
Fig. 6 | ECM elastic and stress-relaxation properties are regulated by the efflux of monovalent ions from ECM samples through altered PG ion binding, while divalent ions stay tightly bound. A stepwise ion concentration gradient between HYPO and ISO was used to investigate changes in ECM samples after 24 h incubation. **a–c**, Under lower baseline osmolality, we observed a greater relative increase in incubation solution osmolality normalized to ECM sample dry weight (showing leakage of ions from ECM samples) (**a**), and increased elastic modulus E (**b**) and faster stress relaxation $\tau_{0.65}$ (**c**) of ECM samples. In **a–c**, solid lines indicate linear regression of a pair of parameters, dotted lines show the associated 95% confidence interval error bands, and correlations were evaluated using two-tailed Spearman's ρ for $n = 4$ biological samples. **d,e**, Collagen fibre structure analysis: collagen axial staggering was analysed from 2D SAXS patterns of Bragg peaks (**d**) and revealed no shifts in intensity peaks (**e**). **f,g**, Analysis of collagen molecule lateral packing from 2D SAXS patterns (**f**) revealed a slight increase in lateral molecule spacing (**g**) within the range of hydrated collagen

fibrils in HYPO condition, suggesting a slightly higher water uptake between collagen molecules. The P value was calculated using a two-tailed t-test for $n = 3$ biological samples. Ion efflux analysis: to further understand the role of PGs in the perifibrillar matrix, the diffusion of selected mono- and divalent ions from the ECM samples in HYPO versus ISO environments was investigated for $n = 3$ biological samples. **h**, Solution osmolality was quantified after 24 h of incubation (24 h) and compared with baseline (base), showing ion efflux from ECM samples in HYPO condition. P values were determined using two-tailed t-tests for $n = 3$ biological samples; significance threshold: $P < 0.05$; NS, not significant. **i**, After 24 h in HYPO, efflux of the monovalent Na^{1+} and Cl^{1-} ions was evident, while no change was observed for divalent Ca^{2+} and Mg^{2+} ions. **j**, After 24 h in ISO, Na^{1+} and Cl^{1-} ions were present in high concentrations (as expected), while Ca^{2+} and Mg^{2+} ions again showed no efflux, suggesting that these divalent ions remained bound inside the ECM samples. In plots **g–j**, whiskers show minimum and maximum values, and middle lines show medians.

---

water-binding strength and swelling could be useful to distinguish different tendon pathologies.

Diffusion of monovalent ions regulates ECM elastic and stress-relaxation properties through PGs

To elucidate how environmental ion concentrations regulate water binding and, consequently, elastic and stress-relaxation properties, we used distinct osmotic concentrations ranging from HYPO to ISO conditions. We observed an increase in the normalized ion efflux from ECM samples with decreasing baseline osmolality (Fig. 6a), reflected by their negative correlation ($\rho = -0.90$, $P < 0.0001$). To verify that the ion effluxes were related to changes in elastic and stress-relaxation properties, ECM mechanics were characterized after incubation. With decreasing baseline osmolality, increasing E (Fig. 6b) and decreasing $\tau_{0.65}$ (Fig. 6c) were quantified, reflected by a negative correlation for E ($\rho = -0.94$, $P < 0.0001$) and a positive correlation for $\tau_{0.65}$ ($\rho = 0.89$, $P < 0.0001$).

To distinguish between potential effects of collagen fibre contraction owing to osmotically induced structural alterations in ECM mechanics in HYPO versus ISO conditions, SAXS was used. The axial staggering of tropomolecules in collagen fibrils results in a periodic pattern of stripes with higher (overlap) and lower (gap) molecule

density that can be imaged by transmission electron microscopy or SAXS[34,35]. The collagen axial staggering was evaluated by analysing the two-dimensional (2D) SAXS patterns, which showed several orders of Bragg peaks (Fig. 6d). The nth q positions ($n = 1, 3, 5...$) can be converted to $D = 2\pi n/q_n$, where D is the intermittent distance (~67 nm) inside the collagen fibrils as indicated by gap and overlap zones. Analysis of the peak positions of signal intensities in the q space showed no relevant shift of peak positions between the HYPO and ISO conditions (Fig. 6e). The absence of a relevant shift between the peaks shows that collagen fibrils were not shortened, suggesting no induced tensile stresses by axially contracting collagen fibres that may have affected ECM mechanics[15]. This observation contrasts with the effects of dehydration (for example, owing to PEG-induced osmotic pressure), which were previously reported to cause collagen contraction[15]. Further, the lateral packing of collagen molecules was analysed from 2D SAXS patterns (Fig. 6f) and revealed a slightly increased spacing in HYPO compared with ISO (Fig. 6g). This indicates a somewhat higher water content in fibrils subjected to HYPO condition.

PGs reside in the perifibrillar matrix around collagen fibre bundles, causing them to separate from each other. To understand the role of PGs in regulating ECM mechanics, we investigated the diffusion of ions out

of ECM samples next. Comparing HYPO versus ISO, first, the ion efflux was measured in terms of osmolality change after incubation (24 h) and with respect to baseline (base) solutions. Osmolality increased only in HYPO, suggesting ion efflux from ECM samples (Fig. 6h). By contrast, there was no change in osmolality after incubation in ISO. Monovalent and divalent cations can bind to the negative charges of PGs and modulate electrostatic effects, such as repulsion[2,3,36]. For example, Na^{1+} can shield electrostatic effects of PGs, and Ca^{2+} can form interchain cross-links between PGs. Subsequently, we measured concentrations of selected ions (that is, Na^{1+}, Cl^{1-}, K^{1+}, Ca^{2+} and Mg^{2+}) in HYPO and ISO solutions after 24 h of ECM sample incubation ($HYPO_{24h}$ and ISO_{24h}). From solution ion concentrations, we aimed to detect potential ion efflux and thus alterations inside ECM samples. Notably, baseline solutions were deionized water (HYPO) and physiological saline solution without Ca^{2+} and Mg^{2+} (ISO). In $HYPO_{24h}$, concentrations of monovalent ions Na^{1+}, Cl^{1-} and K^{1+} were increased, while divalent ions Ca^{2+} and Mg^{2+} remained at very low concentrations (Fig. 6i). This observation suggests that divalent cations mostly remained inside the ECM owing to the higher strength of divalent ion bonds, as expected based on the tight binding found in divalent ions binding to charged surfaces[37], in contrast to monovalent cations diffusing out. In ISO_{24h}, Na^{1+}, Cl^{1-} and K^{1+} were overall at comparably high concentrations (Fig. 6j), which was expected as the baseline ISO solution contained these ions. Interestingly, divalent ions Ca^{2+} and Mg^{2+} remained at very low concentrations in ISO_{24h} as well. The low concentrations of Ca^{2+} and Mg^{2+} in both $HYPO_{24h}$ and ISO_{24h} solutions suggest that their tighter divalent bonds inside the ECM prevented their efflux, despite the abundantly available monovalent cations, such as Na^{1+}, that could have replaced bonds of divalent ions, such as Ca^{2+}.

Discussion

Inflammation or injury of a tissue causes swelling and associated alterations in ECM properties, as observed in tendinopathy. In this work, tendon swelling was selected as a model to investigate related changes in ECM biophysical properties and methods to detect such changes non-invasively. While clear differences between healthy and inflamed tendon can be captured with MRI (Fig. 1), little was known about the physical causes that result in the substantial differential alterations in T_1 and T_2^*. Our systematic study of dissected tissues exposed to defined osmotic environments provides highly valuable insights concerning fundamental ECM properties, thereby enabling a more advanced interpretation of MRI scans. Our data show how osmotic environments differentially regulate ECM swelling, water binding (Fig. 2) and mechanics (Fig. 4). Our findings also unravel the role of the perifibrillar matrix, namely PGs (Fig. 6), and its electrostatic properties in regulating water binding and ECM elastic and stress-relaxation properties. We have shown that the environmental ion concentration regulates water binding, and that the proportion of more loosely bound water in the ECM plays a crucial role in ECM elasticity and stress relaxation (Fig. 4). Our ex vivo ECM model and experimental set-up with osmotic environment modulation enabled parallel characterization of mechanical properties and MRI relaxation parameters (Fig. 2). Therein, we used a well-controlled ECM model based on fresh biological tissue instead of artificial materials to mimic an in vivo setting more accurately, which was supported by an in vivo case study comparing a patient to a healthy control subject. We presented an approach for non-invasive detection of the observed ECM alterations using combined T_1 and T_2^* mapping, and identified their independent correlations with ECM biophysical properties, including swelling, elasticity and stress relaxation. Furthermore, we demonstrated the collagen-independent role of PGs in ECM elastic and stress-relaxation properties (Fig. 6), and that environment ion concentration and osmotic pressure regulate ECM mechanics differently (Fig. 5). We believe that our findings may help to advance methods for non-invasive detection of local ECM alterations in pathologies involving dysregulations of osmotic environments, PGs in the

perifibrillar matrix, swelling and water binding, as well as the development of synthetic biomaterial-based therapies.

The observed increased elastic modulus and enhanced stress relaxation of ECM samples in conditions with increased water-binding strength is a particularly important finding as stress-relaxation properties of physiological, viscoelastic ECM were previously identified as a crucial driver for cell–matrix interactions (for example, stem cell fate decision in regeneration)[21,22]. On the contrary, decreased stress relaxation, observed in conditions with decreased water-binding strength, was previously related to pathological ECM degeneration[38–40] and may also be related to dysregulated water binding (that is, electrostatic) properties. The elastic modulus was previously found to regulate the abovementioned governing cell functions[41], and its various roles in physiology continue to be investigated. In the context of HYPO environments, a recent study reported that osmotic changes influence cell-fate decision in regeneration using viscoelastic ECM-mimicking hydrogels[18]. However, that study did not consider potential effects of decreased environmental ion concentration on ECM stress-relaxation properties, although enhanced stress relaxation could have stimulated cells similarly[18].

To understand the causes of the strong alterations in ECM mechanics observed for altered environmental ion concentration (that is, HYPO versus ISO), common paradigms might have considered influences of load-bearing collagen fibres (that is, osmotic pressure-induced tensile stress[15]) or cells, either actively (for example, contractile forces[42]) or passively (for example, protein-phosphorylating cytosolic enzymes[43]). However, SAXS analyses of collagen molecule axial staggering and lateral packing revealed that collagen likely did not contribute to the observed alterations in ECM mechanics. This finding was in agreement with that from a previous study showing that collagen fibres in aqueous solutions relax to maximum length at zero and low ion concentrations[44]. Cellular influences were considered negligible as storage and incubation conditions (that is, low temperatures, without nutrients) likely rendered cells apoptotic or inactive, and impaired efficient enzyme function. Moreover, differences in ECM mechanics were maintained after alternating exposure to HYPO (dH_2O) and ISO solutions, likely leaving cells apoptotic. Further, cells would not be able to cause the observed strong changes in ECM mechanics even in ideal culture conditions[42]. In line with this notion, a previous study on mineralized tissue reported that increased amounts of bound water enhanced bone mechanical properties, such as toughness, with the underlying mechanism being cell-independent[45].

By investigating the diffusion of selected ions that can affect PG function, the role of PGs in ECM elastic and stress-relaxation properties was shown (Fig. 6). Ion efflux from ECM samples correlated with alterations in elastic modulus and stress relaxation. A notable efflux of monovalent cations, such as Na^{1+}, in low osmolality (that is, HYPO) condition increased negative charge effects by PGs, leading to a decreased proportion of more loosely bound water in the perifibrillar PG matrix[2,3,36]. The negative charge of PGs is generated predominantly by their numerous subunits, such as chondroitin sulfate (CS) chains[3], and increased negative charge effects were previously reported to result in stacking of CS chains owing to electrostatic repulsion[36]. By contrast, measurements of divalent cations suggested that Ca^{2+} ions, for example, stayed bound inside ECM samples where these can form transient non-covalent interchain cross-links between the negatively charged PGs[36], which can affect ECM stress-relaxation properties[21]. Our data suggest that in conditions of increased PG negative charge effects (for example, HYPO), electrostatic repulsion between PGs causes increased steric hindrance and increases the flexibility of the dynamic interchain cross-links by physical ion bridges (for example, by Ca^{2+}), which consequently increases ECM stress relaxation under mechanical load[21] (Fig. 7). Further, the data suggest that increased electrostatic repulsion between PG negative charges results in increased compressive resistance of the ECM samples. This notion is supported by

(i) CS chain stacking acts as steric hindrance and leads to easier slipping of dynamic interchain cross-links

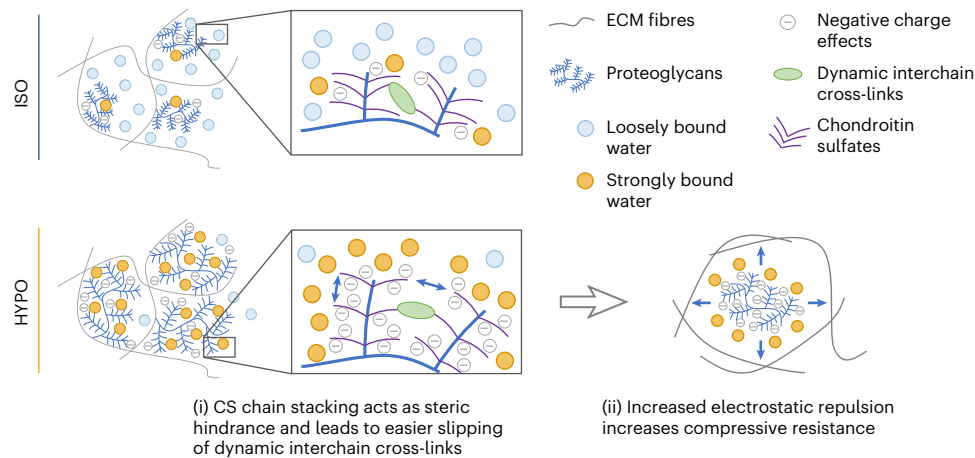(ii) Increased electrostatic repulsion increases compressive resistance

Fig. 7 | Proposed mechanism how PGs regulate ECM elastic and stress-relaxation material properties, revealed by modulating the ion concentration of the osmotic environment. Compared with ISO, the proportion of more loosely bound water in the ECM was lower in HYPO conditions. Ion diffusion experiments suggest increased negative charge effects of PGs owing to leakage of monovalent cations from the ECM that would otherwise shield electrostatic effects of negatively charged PGs, while divalent ions stay tightly bound, suggesting that they form physical bridges between negatively charged PGs (transient interchain cross-linking). Electrostatic repulsion forces (two-headed blue arrows) acting between the more negatively charged PG subunits (for example, CS chains) can lead to CS chain stacking and thus increased distancing and enlarged PGs. (i) This increased distancing can cause faster slipping of dynamic interchain cross-links (for example, ionic bridges/bonds by Ca^{2+}) between PGs under load. (ii) ECM network with more negatively charged PGs, thereby binding more water strongly, increases the compressive resistance (one-headed blue arrows) of the ECM under load owing to increased electrostatic repulsion between PGs.

the analysed efflux of counterions in HYPO (Fig. 6h,i) and the increased water-binding strength (Fig. 2f,h), and in line with a previous study reporting the relevant contribution of electrostatic properties to the elastic modulus in cartilage[3].

Dynamic microscopic ECM properties, particularly stress-relaxation mechanical characteristics, have gained considerable attention recently in tissue engineering for enabling cells to actively remodel their surroundings and instructing fate decisions in cell niches[22,46]. These ECM properties expand the range of more established structural ECM properties, such as load-bearing (collagen) fibre structures that provide stability and scaffolding functions[22,46]. ECM stress-relaxation properties are often considered to be regulated by the extent of covalent cross-linking in a matrix. Hygroscopic properties have been considered mainly as a prerequisite to yield a hydrated fibre network for mimicking natural ECM (for example, with hydrogels)[46]. However, the results presented here emphasize the role of the perifibrillar (PG-rich) matrix in directly regulating ECM stress relaxation. In this context, we propose that the function of PGs as key regulators of ECM water binding and electrostatic properties may expand the list of mechanobiological cues for cell–matrix interactions (for example, mechanics, fibre structure, porosity and topography). The water-binding function of PGs, or glycosaminoglycans, is governed by negatively charged groups[3], such as sulfate groups, which are dysregulated in several pathologies. Examples include perineuronal nets in Alzheimer's disease[47,48], the disorganization of collagen fibril spacing in macular corneal dystrophy[49,50], and pro-inflammatory or anti-inflammatory effects[51,52]. The link between altered sulfation (and thus charge) properties and ECM mechanics has been understudied. Disease modelling of pathologies involving dysregulations of PG function, osmotic environments or swelling can be potentially improved using ECM-mimicking materials that allow to modulate water-binding strength, or polyelectrolyte, properties. In addition, the water-binding properties of the ECM (for example, charged groups) could also be actively modulated by cells residing in the ECM[47]. Such perspectives could open up new avenues for investigating the role of water binding in (mis)guiding cell behaviour and for potentially identifying new therapeutic targets.

While MRI allows to distinguish inflamed ECM (for example, in tendinopathy) from healthy ECM, it is difficult to non-invasively detect associated mechanical changes. Understanding the local mechanical competence of the tissue could help to unravel the causes for poor tendon healing outcomes that many patients experience. A previous study on healthy Achilles tendon investigated changes in hydration after physical activity with MRI using the off-resonance saturation ratio, and reported a loss of free water molecules and decreased tendon volume[53] but did not measure tissue mechanical properties. In the high-resolution MR images (Fig. 3), striation patterns of fascicle edges were clearly visible in HYPO owing to the expanded IF matrix, which was not the case in FRESH and ISO where striations were barely visible or not visible at all. In the quantification of MRI relaxation parameters using whole-body MRI scanners, we observed higher T_2^* values in Achilles tendon from in vivo human scans compared with ex vivo ovine scans. This difference is likely attributable to technical aspects of imaging (for example, potential overestimation of T_2^* in the in vivo tendon owing to sparse echo sampling) and differences in tendon composition and/or structure influenced by mechanical loading-induced tissue adaptations[54–59]. In addition, this difference could be driven by the tissue region from which T_2^* was quantified: in the in vivo scans, all three bands (subtendons) of the human Achilles tendon[60], including the separating loose connective tissue, were imaged; in the ex vivo scans, ECM samples excised from only one band (gastrocnemius, without surrounding loose connective tissue) were analysed. Possible differences in trace elements, such as iron, might also influence T_2^* values in tendon[61–63]. Notably, the MRI scans of the ex vivo ECM samples were performed at room temperature and would likely yield higher values for the relaxation parameters in tissues in vivo at body temperature (Extended Data Fig. 7). Our findings allow an improved interpretation of MRI data using combined T_1 and T_2^* mapping, leveraging a link between PG water binding and ECM swelling and mechanics (E, $\tau_{0.65}$). For example, in our in vivo case study (Fig. 1), MRI of the patient's pathological Achilles tendon could be interpreted as severe swelling with compromised mechanical properties, indicating altered tissue composition and impaired functionality. The patient's contralateral and presumably healthy Achilles tendon showed
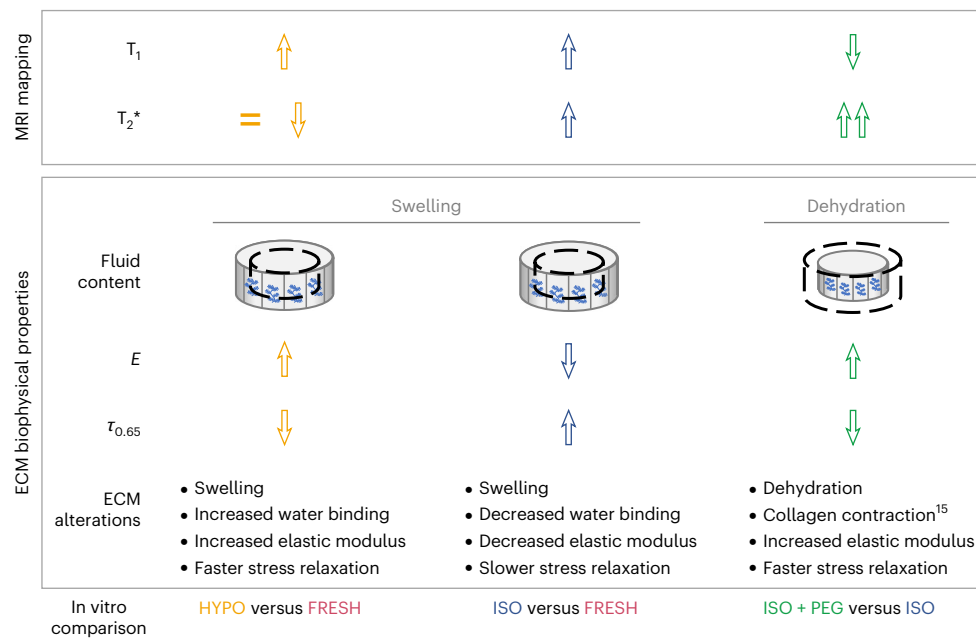
Fig. 8 | Summary illustrating the potential of combined T_1 and T_2^* mapping for improving diagnostics in swelling-associated ECM changes. The ECM alterations in MRI and ECM biophysical parameters between the in vitro conditions, HYPO versus FRESH (left), ISO versus FRESH (middle) and ISO + PEG versus ISO (right), are shown. The results of the in vitro study show how combined MRI T_1 and T_2^* mapping could potentially be used to provide additional insight into ECM changes in swelling/dehydration, water binding/collagen fibres, elastic modulus and stress-relaxation properties. Understanding the biophysical meaning of such changes in characteristic MRI parameters could eventually enable the detection of alterations in mechanical or structural tissue properties and lead to improved diagnostics and clinical decision-making. Top panel: characteristic changes in MRI T_1 and T_2^* caused by specific osmotic modulation. Bottom panel: alterations in ECM biophysical properties related to the characteristic MRI parameter changes.

an increase in T_1 only, suggesting pathological alteration characterized first by inflammatory swelling caused by cytokine-mediated exudation. Mechanical properties, and thus tissue functionality and composition, appeared maintained. Such insight could support orthopaedic surgeons in prescribing a suitable therapeutic approach to the patient, for instance, through personalized physiotherapy addressing compensatory gait mechanics and aberrant loading patterns that may have led to the pathological tissue alterations in the unaffected contralateral foot. Another potential application is the improvement of surgical interventions for degenerated or ruptured Achilles tendon. So far, it is not well understood why for some patients healing of sutured ends of a tendon leads to scarring or non-union, accompanied by diminished mechanics and functionality. Our data could facilitate monitoring of healing progress after surgery, and help recognize and categorize impaired tissue regeneration earlier. This could allow for improved clinical decision-making before substantial tissue degeneration, when intervention success rates may be greater, by adapting physiotherapy protocols or opting for corrective surgery. Possibly, our data could also facilitate an enhanced detection of dysregulated ECM properties in oedema[8,9]. Furthermore, we showed clearly distinguishable characteristics in MRI for osmotic pressure (PEG) induced ECM dehydration compared with altered water binding (that is, HYPO versus ISO). For instance, previous studies have shown that expanding solid tumours compress and dehydrate surrounding soft tissue[12,33]. The relationships between changes in MRI T_1 and T_2^* parameters and alterations in ECM biophysical properties presented in this work are summarized in Fig. 8. The schematic overview may support the use of our findings to eventually detect alterations in ECM biophysical properties associated with tissue regeneration or disease-specific degeneration using combined T_1 and T_2^* mapping; the underlying MRI data are summarized in Extended Data Fig. 8. ECM water binding and other biophysical properties (for example, swelling and mechanics) are important markers in various pathologies (for

example, viscoelasticity in glioblastoma[39], hypertension[40] and intervertebral disk[38]; fluid accumulation in lung inflammation[7], swelling[8] and oedema[8,9]) and in regeneration (for example, return to sport after surgery, personalized therapy and judging therapy impact).

Intrinsic to exploiting model systems are their limitations. Our ex vivo model is only addressing a limited number of parameters, such as swelling and water binding in relation to mechanical properties, and not the full set of potential ECM alterations that may occur during in vivo pathological degenerations. Indeed, the ex vivo ECM model was artificially modified in its biophysical properties by tuning the swelling and water binding (that is, electrostatic) properties via environmental osmolality. These inherent osmotic, or electrostatic, properties of the ECM are mainly governed by negative charges of PGs, which are established, for example, on CS by fixed ionic carboxyl and sulfate groups. In pathological ECM alterations, a disturbed collagen fibre network is frequently reported, but also dysregulations of PG sulfation have been found in various pathologies[48,64]. However, altered PG charge effects have rarely been related to ECM mechanics, despite the high relevance of ECM elastic and stress-relaxation properties for cell–matrix interactions in regeneration[21] or disease[65,66]. Another example of altered osmotic properties in more complex pathological tissue degeneration is osteoarthritis, where collagen fibres in the cartilage fibre-composite matrix are degraded, leading to reduced restriction of the water-attracting PGs. The resulting tissue swelling can lead to decreased fixed charge densities when the same number of PGs are located in an inflated ECM volume, resulting in equivalent osmolality changes of 150 mOsm (ref. [67]). This may represent a parallel to the substantial swelling (~75% volume increase) reported in Achilles tendinopathy together with decreased mechanical properties[68], and to the swelling and diminished mechanics in ISO versus FRESH condition in our ECM model (Fig. 4). Moreover, increasing the electrostatic effects in our ECM model by an osmolality decrease of 150 mOsm relative to ISO condition resulted in

substantial changes in elastic and stress-relaxation properties (Fig. 6). This observation is consistent with a previously reported relationship between PG concentration (that is, fixed charge density) and elastic modulus[2]. Further work is required to better understand how the complexity of altered ECM composition and structures, and also cellular contributions, link to altered osmotic properties and to quantitative MRI parameters.

This work demonstrates the crucial role of water-binding features for elastic and stress-relaxation characteristics of the ECM. Osmotic environments were shown to modulate the ECM water-binding properties and suggest an important role of PGs to regulate proportions of more loosely bound water in tendon tissue. Our investigations revealed independent correlations of MRI T_1 and T_2^* with ECM swelling, as well as elastic and stress-relaxation properties, demonstrating the potential of their combined application to discriminate pathological tissue alterations related to dysregulated swelling, water binding or osmotic environments. Future work should investigate this potential application with ex vivo tissue probes of pathologically degenerated tissue and in vivo scans from a larger cohort of patients, as well as the reasons for differences in T_2^* values between MRI scans of ex vivo animal and in vivo human tissue. Shedding light on the interplay between water binding and ECM mechanics may lead to new tissue engineering strategies involving biomaterials with controllable hygroscopic properties as one dynamic microscopic design parameter.

Methods

The part of this work involving human participants was approved by the Ethics Board of the Charité - Universitätsmedizin Berlin (EA2/088/16). All subjects provided written informed consent. For the ex vivo analyses, tissue samples were collected from animals after euthanasia in compliance with the ethical guidelines of legal, local animal rights protection authorities (Landesamt für Gesundheit und Soziales Berlin). To keep the number of animals to a minimum, the samples were taken from other research projects but with no relationship that would affect tissue properties of the samples (G0424/17 and G0210/18).

In vivo scans

In vivo imaging was performed with a clinical 3 T whole-body MRI scanner (MAGNETOM Vida, software XA20A, Siemens Healthineers) using a 16-channel measurement coil for foot and ankle scans as commonly used in clinical application (Foot/Ankle 16, Siemens Healthineers). Imaging was performed separately for each foot in three individuals: one healthy asymptomatic control subject (male, 34 years old) without known pathologies (CTRL), and two patients (female, 53 years old; male, 48 years old) with mid-portion Achilles tendinopathy (PATHO) diagnosed by a senior consultant for surgery (S.T.) (Supplementary Fig. 1a). The same UTE imaging sequence (described in more detail below) was used for the in vivo and ex vivo measurements, with five flip angles ranging between 5° and 24° for variable flip angle (VFA)-based T_1 mapping and three echoes with echo times (TE) ranging from 0.1 ms to 4.8 ms for T_2^* mapping. The UTE sequence was optimized for image acquisition of tendon tissue, potentially resulting in erroneous T_2^* values for non-tendon tissues with transverse relaxation times clearly longer than 5 ms. Fewer echoes were selected compared with the ex vivo acquisition to reduce acquisition time and patient discomfort. Both acquisitions used spatial resolution of $1.2 \times 1.2 \times 3.5$ mm³, rectangular hard-pulse excitation with 100 µs pulse duration and acquisition bandwidth of 1,076 Hz per pixel, with a repetition time (TR) of 12 ms for T_1-related and 8 ms for T_2^*-related data acquisitions. Data analysis and T_1 correction for relaxation during the radio frequency pulse were performed as in the ex vivo analysis. For one patient (male, 48 years old), the foot with tendinopathy was scanned additionally with standard clinical T_1-weighted and proton density (PD)-weighted sequences for comparison with UTE sequence results (Extended Data Fig. 2).

Ex vivo ECM model

Fresh Achilles tendons were excised from 16 healthy sheep (Merino, female, 4+ years old). The tissue samples were subdivided into different experiments, as shown in Supplementary Fig. 1b. To avoid dehydration, tendons were enveloped in plastic wrap, placed in a moist environment immediately after excision and stored at 4 °C until dissection and testing. A moist environment was established by placing each tendon in a sealed 50 ml polypropylene centrifuge tube with water-moistened cotton gauze at the conical tip of the tubes. An excised Achilles tendon consisted of two distinct bands of fibrous tissue connecting each of the gastrocnemius and soleus muscles via the enthesis to the bone. The gastrocnemius band was used owing to its mostly elongated cylindrical shape, allowing for similar ECM sample sizes and better tissue handling during characterization (for example, fibre direction for MRI and parallel planes for mechanical characterization). Tendon samples from the contralateral limbs were assumed to have comparable tissue properties to the ipsilateral limbs. To avoid cartilaginous or calcified structures near the enthesis, diverse fibre directions in the transition from mid-tendon to enthesis, or myofibrous structures near the muscle, only the mid-portion of a tendon was used. The tendon mid-portion was defined between ~2.5 cm and ~5 cm proximal to the enthesis. Each tendon mid-portion was then dissected cross-sectionally into six to eight cylindrical ECM samples of ~3 mm thickness and ~6.2 mm diameter. The elongated shape, ordered structure and consistent tissue properties of the tendon mid-portion allowed the variability of ECM structure and components to be minimized. The PG concentration of ECM samples was quantified with ~0.1% of tendon dry weight using a DMMB assay (280560-N, AMSBIO) after tissue digestion by papain (280560-TDK, AMSBIO), which was in a similar range as previously reported for rabbit Achilles tendon[69]. As MRI relaxation parameters can be affected by freeze–thawing[70] or fixation[71], ECM samples were characterized in FRESH condition or after incubation of fresh ECM samples in different ion buffers. All ECM sample characterizations were carried out at room temperature.

Osmotic environment modulation

Mechanical and MRI characterizations were performed directly after dissection (that is, FRESH condition) and again after swelling in different osmotic environments for 24 h, as depicted in Supplementary Fig. 3. For exposure to different osmotic environments, a 15 ml tube containing 8 ECM samples held by 3D-printed polylactic acid (PLA) inlays that allowed contactless sample positioning and unconfined swelling (Fig. 2b) was filled with 13 ml of the respective solution. To tune ECM properties through the osmotic environment of a sample (that is, the ion concentration of the bath solution), the HYPO environment was established with deionized water and the ISO environment with physiological saline solution without Ca^{2+} and Mg^{2+} (D8537, Sigma-Aldrich) with a pH value ~7. For hyper-osmolar environments, osmolality was either increased by adjusting the saline concentration for higher ion concentrations or by adding macromolecules for dehydration of ECM samples by osmotic pressure. For higher ion concentration, saline concentrations were increased by 27% and 100% (double ISO osmolality). Van't Hoff's equation was used to determine the osmotic pressure in pascals $\pi = cRT$, with c, R and T representing the osmolar concentration of the solute (van't Hoff factor of osmotically active particles times molar concentration of the dissolved salt), the gas constant and the absolute temperature, respectively. For these calculations, we used the simplifying assumption that the ion concentration in ISO solution was comparable to that of isotonic 0.9% NaCl saline solution, which resulted in an approximate equivalent osmotic pressure of ~744 kPa. Accordingly, increases in ion concentration by 27% and 100% corresponded to osmotic pressure increases of ~200 kPa and ~744 kPa, respectively. For dehydration, 5 kDa PEG molecules (06679, Sigma-Aldrich), expected to be unable to diffuse into the ECM samples, were added to the swelling solutions, thereby applying osmotic pressure[15]. For PEG in aqueous

solutions, osmotic pressure was calculated using a nonlinear relation as described by Money[72]. Accordingly, PEG concentrations of 91 g l^{−1} and 125 g l^{−1} yielded osmotic pressures of ~100 kPa and ~200 kPa, respectively.

MRI UTE imaging for T_1 and T_2^* mapping

MRI scans to characterize ECM samples in FRESH condition were performed after 3 days of storage and, subsequently, after 24 h exposure to different osmotic environments. To avoid dehydration of ECM samples in FRESH condition during the MRI scans taking 1–3 h, water-moistened gauze was placed in the bottom of a sealed 15 ml tube carrying a PLA inlay without contact to ECM samples (Extended Data Fig. 9). The 3D-printed PLA inlays served as a mounting device to hold ECM samples in parallel contactless positions[73] (Fig. 2b). For MRI data acquisition, multiple tubes containing all ECM samples at a given time point were measured simultaneously by adjacent and parallel positioning of tubes, which were wrapped between the two elements of a 16-channel flexible measurement coil (Variety, NORAS MRI Products). Measurements were performed with a clinical 3 T whole-body MRI scanner (MAGNETOM Prisma Fit, software VE11B and XA30A, Siemens Healthineers). Samples were placed with the fibre orientation parallel to the main magnetic field to reduce the influence of magic angle effects on T_2^* relaxation times[74]. To mitigate the problem of rapid signal decay of tendon tissue, an in-house developed 3D UTE imaging sequence was used[75]. To estimate longitudinal T_1 relaxation times, repeated 3D UTE acquisitions were performed using the VFA technique[76] with eight different excitation flip angles between 5° and 39°; rectangular hard-pulse excitation with 260 μs pulse duration; a TE of 0.150 ms; and a TR of 5.5 ms. To account for relaxation during the radio frequency pulse, a modified Ernst equation was used to fit T_1 from the VFA data[77]. The transverse relaxation time T_2^* was estimated by acquiring eight gradient-recalled echoes at different TEs between 0.150 ms and 3.0 ms by combining echo-train shifting[78] and multiple gradient refocused echoes within each readout train[79] and using a constant flip angle of 8° with a TR of 6.0 ms. Other acquisition parameters were identical for both T_1 and T_2^*: isotropic spatial resolution of $0.8 \times 0.8 \times 0.8$ mm³, acquisition bandwidth of 941 Hz per pixel and two averages for improved signal-to-noise ratio. Images were reconstructed offline in MATLAB (The MathWorks) version R2019b using re-gridding with iterative sampling density compensation and an optimized kernel[80]. Owing to limited signal-to-noise ratio and signal decay sampling, only mono-exponential fitting of T_2^* was performed. While bi-exponential fitting of T_2^* decay curves offers the potential to distinguish between more loosely and more strongly bound water[81], the ex vivo MRI scans did not reveal any bi-component signal (Extended Data Fig. 10). Data analysis and nonlinear curve fitting to estimate relaxation parameters were also performed in MATLAB. After calculating relaxation parameter maps, circular/elliptical regions of interest were drawn manually in the central transverse slice of each disk. The T_1 and T_2^* relaxation times extracted from all voxels were averaged for each region of interest. PD mapping[82] was not performed as it requires several correction factors and calibration scans for quantification in combination with appropriate UTE-based sequences that can cope with the rapid signal decay and were not available at the time of the study.

Swelling measurements

Gravimetric swelling was measured using a calibrated balance (LC621S, Sartorius). The fresh mass of a sample was measured immediately after sample dissection. For swelling curves, swelling was recorded for 28 h with repeated measurements of five samples per condition (that is, HYPO and ISO) from one animal. For the swollen state measurements, excess fluid was removed by gently patting the lower edge of the ECM samples onto a sheet of paper. Swelling was defined as swelling (%) = $(m_{\mathrm{swollen}} - m_{\mathrm{fresh}})/m_{\mathrm{fresh}}$.

Histological analysis of tissue organization

Representative ECM samples from FRESH, HYPO and ISO conditions were embedded in fresh freezing compound (Tissue-Tek O.C.T., Sakura) and frozen in liquid nitrogen-cooled isopentane (Carl Roth). Subsequently, frozen samples were stored at −80 °C until cryo-sectioning. Samples were sectioned at 7 μm thickness and sections were placed onto glass slides (SuperFrost Ultra Plus, Menzel-Gläser). Histological analysis was performed by H&E and AB stainings. Imaging was performed using bright-field microscopy at 20× magnification.

MRI high-resolution structural imaging

High-resolution structural imaging was performed on representative ECM samples first in FRESH and then again after 24 h swelling in HYPO and ISO conditions using a 9.4 T MRI small animal scanner (BioSpec USR 94/20, Bruker) with a horizontal bore of 20 cm, a gradient system of 660 mT m^{−1} and ParaVision 6.0.1 operating software (BioSpin, Bruker). In addition, a vendor-supplied two-channel quadrature cryoprobe was used to optimize the signal-to-noise ratio. Samples were deliberately oriented along the magic angle using a custom 3D-printed laboratory tube insert with planes angled at 54.7°. Images were acquired using a vendor-supplied 2D multi-slice Cartesian gradient-echo sequence with 70×70 μm² in-plane spatial resolution; 3.1 ms TE; 1,200 ms TR; 8 averages; 75° excitation flip angle; 100 kHz acquisition bandwidth; 32 slices with a thickness of 200 μm; and a total acquisition time of 35 min. Voxels with high signal intensity (light colour) corresponded to tissue regions with increased water accumulation.

Biomechanical testing

ECM elastic and stress-relaxation properties were quantified by elastic modulus and stress-relaxation time by uniaxial unconfined compression (TestBench LM1 system, BOSE) using a 250 g load cell (Model 31 Low, Honeywell)[2]. The compression step was conducted with minimal pre-load, at 0.016 mm s^{−1} and to a maximum strain of 15% along the longitudinal axis of the cylindrical samples. A sample was characterized only once. The loading direction was aligned with the overall ECM fibre orientation to minimize effects of fibre tensile loading and focus on effects of PG-dominated water binding on ECM elastic and stress-relaxation properties. At maximum compression, the stamp position was held constant to record the stress relaxation. The cross-sectional area of a sample was measured from images acquired with a 1,200 dpi resolution with a digital scanner (Perfection V200, Epson) using ImageJ version 1.54f. The maximum compression was limited to 15% strain of tissue sample height[21], which is in the range of strains typically exerted by cells on their surrounding ECM[83]. The elastic modulus E was calculated from the slope of a 5% interval of the linear region of the stress-strain curve. The stress-relaxation behaviour was quantified with $\tau_{0.50}$ and $\tau_{0.65}$, which were defined by the time until 50% and 35%, respectively, of the peak stress at maximum compression was released. The testing protocol restricted the recording of stress-relaxation times to 500 s, as it was previously shown that ECM stress-relaxation properties of $\tau_{0.50} \geq 500$ s affect cell–matrix interactions similar to slow-relaxing, predominantly elastic ECM[21]. Considering that cells sense and respond to fast ECM stress-relaxation properties when applying traction forces at timescales of seconds and minutes[84], we introduced $\tau_{0.65}$ to analyse the early stress-relaxation behaviour. $\tau_{0.50}$ was reported to facilitate relating our results of changes in ECM stress relaxation to those of other studies as it is a frequently used readout in the biomaterials and tissue engineering community[21].

Osmotic gradient and ion diffusion measurements

ECM samples were dissected as described above from fresh Achilles tendons that were excised from five healthy sheep (male, 3 years old) immediately after euthanasia at a local abattoir. Four tendons from two of the animals were used for osmotic gradient studies. Defined

HYPO conditions were achieved by diluting saline solution used for ISO condition with deionized water in 25% increments. Osmolality was measured using a freezing-point osmometer (OSMOMAT Auto, Gonotec). ECM samples were exposed individually to the solutions in 2 ml tubes for 24 h and at the same sample to fluid volume ratio as described above. Subsequently, solution osmolality was measured again to determine osmolality changes owing to ion efflux from samples. Elastic and stress-relaxation properties were quantified using uniaxial compression, as described above. ECM samples were freeze-dried to measure their dry weight, normalize changes in solution osmolality and obtain normalized ion efflux. For ion diffusion measurements, ECM samples were dissected from the other three animals as described above and were subsequently exposed to HYPO and ISO solutions. Solution osmolality was measured at baseline before (base) and after 24 h exposure (24 h) of the ECM samples. To measure the efflux of selected monovalent and divalent ions from ECM samples, HYPO and ISO solutions were analysed after 24 h. Ion concentrations were quantified using the ion-selective electrode method for Na^+, Cl^{1-} and K^{1+} and photometric assay for Ca^{2+} and Mg^{2+}.

Collagen fibre contraction analysis

The SAXS measurements were performed with a Bruker Nanostar 2 using a 2D Vantec-2000 maintenance-free detector at a wavelength of 1.5418 Å (Cu Kα). The focal spot size of the beam was 115 μm and the sample-detector distance was 28.10 cm. We measured the SAXS signal for three samples per condition at five randomly chosen points per condition. ECM samples were dissected from tendons of three animals. These were the contralateral tendons from the animals used for ion diffusion measurements, as described above, and assumed to have comparable tissue properties.

Statistical analysis and plotting

Statistical significance was set at $P < 0.05$; P values indicating non-significant differences were indicated by NS ($P > 0.05$). Values in brackets in the paper represent the mean of quantified values for a given condition. Statistical analyses were performed using GraphPad Prism (version 9.5.1).

Reporting summary

Further information on research design is available in the Nature Portfolio Reporting Summary linked to this article.

Data availability

The main data supporting the results in this study are available within the paper and its Supplementary Information. The raw and analysed datasets generated during the study are available for research purposes from the corresponding author on reasonable request. Source data are provided with this paper.

References

1. Fullerton, G. D. & Amurao, M. R. Evidence that collagen and tendon have monolayer water coverage in the native state. *Cell Biol. Int.* **30**, 56–65 (2006).
2. Mow, V. C., Ratcliffe, A. & Robin Poole, A. Cartilage and diarthrodial joints as paradigms for hierarchical materials and structures. *Biomaterials* **13**, 67–97 (1992).
3. Buschmann, M. D. & Grodzinsky, A. J. A molecular model of proteoglycan-associated electrostatic forces in cartilage mechanics. *J. Biomech. Eng.* **117**, 179–192 (1995).
4. Ehrlich, S. et al. The osmotic pressure of chondroitin sulphate solutions: experimental measurements and theoretical analysis. *Biorheology* **35**, 383–397 (1998).
5. Schwartz, N. B. & Domowicz, M. S. Proteoglycans in brain development and pathogenesis. *FEBS Lett.* **592**, 3791–3805 (2018).
6. Gordon, A. M., Huxley, A. F. & Julian, F. J. The variation in isometric tension with sarcomere. *J. Physiol.* **184**, 170–192 (1966).
7. Gill, S., Wight, T. N. & Frevert, C. W. Proteoglycans: key regulators of pulmonary inflammation and the innate immune response to lung infection. *Anat. Rec.* **293**, 968–981 (2010).
8. Wiig, H. Pathophysiology of tissue fluid accumulation in inflammation. *J. Physiol.* **589**, 2945–2953 (2011).
9. Hashemi, H. S. et al. Assessment of mechanical properties of tissue in breast cancer-related lymphedema using ultrasound elastography. *IEEE Trans. Ultrason. Ferroelectr. Freq. Control* **66**, 541–550 (2019).
10. Nia, H. T. et al. Solid stress and elastic energy as measures of tumour mechanopathology. *Nat. Biomed. Eng.* **1**, 0004 (2017).
11. Nikitovic, D. et al. Proteoglycans-biomarkers and targets in cancer therapy. *Front. Endocrinol.* **9**, 69 (2018).
12. Nia, H. T., Munn, L. L. & Jain, R. K. Physical traits of cancer. *Science* **370**, eaaz0868 (2020).
13. Hsu, C. K. et al. Mechanical forces in skin disorders. *J. Dermatol. Sci.* **90**, 232–240 (2018).
14. Varedi, M., Tredget, E. E., Ghahary, A. & Scott, P. G. Stress-relaxation and contraction of a collagen matrix induces expression of TGF-β and triggers apoptosis in dermal fibroblasts. *Biochem. Cell Biol.* **78**, 427–436 (2000).
15. Masic, A. et al. Osmotic pressure induced tensile forces in tendon collagen. *Nat. Commun.* **6**, 5942 (2015).
16. Dolega, M. E. et al. Extra-cellular matrix in multicellular aggregates acts as a pressure sensor controlling cell proliferation and motility. *eLife* **10**, e63258 (2021).
17. Li, Y. et al. Compression-induced dedifferentiation of adipocytes promotes tumor progression. *Sci. Adv.* **6**, eaax5611 (2020).
18. Lee, H. P., Stowers, R. & Chaudhuri, O. Volume expansion and TRPV4 activation regulate stem cell fate in three-dimensional microenvironments. *Nat. Commun.* **10**, 529 (2019).
19. Murray, J. F. Pulmonary edema: pathophysiology and diagnosis. *Int. J. Tuberc. Lung Dis.* **15**, 155–160 (2011).
20. Vining, K. H. & Mooney, D. J. Mechanical forces direct stem cell behaviour in development and regeneration. *Nat. Rev. Mol. Cell Biol.* **18**, 728–742 (2017).
21. Chaudhuri, O. et al. Hydrogels with tunable stress relaxation regulate stem cell fate and activity. *Nat. Mater.* **15**, 326–334 (2016).
22. Chaudhuri, O., Cooper-White, J., Janmey, P. A., Mooney, D. J. & Shenoy, V. B. Effects of extracellular matrix viscoelasticity on cellular behaviour. *Nature* **584**, 535–546 (2020).
23. Fullerton, G. D. & Rahal, A. Collagen structure: the molecular source of the tendon magic angle effect. *J. Magn. Reson. Imaging* **25**, 345–361 (2007).
24. Bag, M. A. & Valenzuela, L. M. Impact of the hydration states of polymers on their hemocompatibility for medical applications: a review. *Int. J. Mol. Sci.* **18**, 1422 (2017).
25. Rorschach, H. E., Lin, C. & Hazlewood, C. F. Diffusion of water in biological tissues. *Scanning Microsc. Suppl.* **5**, S1–S9 (1991).
26. Lattanzio, P. J., Marshall, K. W., Damyanovich, A. Z. & Peemoeller, H. Macromolecule and water magnetization exchange modeling in articular cartilage. *Magn. Reson. Med.* **44**, 840–851 (2000).
27. Nebelung, S. et al. Ex vivo quantitative multiparametric MRI mapping of human meniscus degeneration. *Skeletal Radiol.* **45**, 1649–1660 (2016).
28. Ma, Y. J., Chang, E. Y., Bydder, G. M. & Du, J. Can ultrashort-TE (UTE) MRI sequences on a 3-T clinical scanner detect signal directly from collagen protons: freeze-dry and D_2O exchange studies of cortical bone and Achilles tendon specimens. *NMR Biomed.* **29**, 912–917 (2016).
29. Bachmann, E. et al. T1- and T2*-mapping for assessment of tendon tissue biophysical properties: a phantom MRI study. *Invest. Radiol.* **54**, 212–220 (2019).

30. Andreisek, G. & Weiger, M. T2* mapping of articular cartilage: current status of research and first clinical applications. *Invest. Radiol.* **49**, 57–62 (2014).

31. Thorpe, C. T. & Screen, H. R. C. Tendon structure and composition. *Adv. Exp. Med. Biol.* **920**, 3–10 (2016).

32. Werbner, B. et al. Saline-polyethylene glycol blends preserve in vitro annulus fibrosus hydration and mechanics: an experimental and finite-element analysis. *J. Mech. Behav. Biomed. Mater.* **125**, 104951 (2021).

33. Fernández-Sánchez, M. E. et al. Mechanical induction of the tumorigenic β-catenin pathway by tumour growth pressure. *Nature* **523**, 92–95 (2015).

34. Masic, A. et al. Multiscale analysis of mineralized collagen combining X-ray scattering and fluorescence with Raman spectroscopy under controlled mechanical, thermal, and humidity environments. *ACS Biomater. Sci. Eng.* **3**, 2853–2859 (2017).

35. Ping, H. et al. Mineralization generates megapascal contractile stresses in collagen fibrils. *Science* **376**, 188–192 (2022).

36. Horkay, F., Basser, P. J., Hecht, A. M. & Geissler, E. Chondroitin sulfate in solution: effects of mono- and divalent salts. *Macromolecules* **45**, 2882–2890 (2012).

37. Lochhead, M. J., Letellier, S. R. & Vogel, V. Assessing the role of interfacial electrostatics in oriented mineral nucleation at charged organic monolayers. *J. Phys. Chem. B* **101**, 10821–10827 (1997).

38. Inoue, N. & Espinoza Orías, A. A. Biomechanics of intervertebral disk degeneration. *Orthop. Clin. North Am.* **42**, 487–499 (2011).

39. Streitberger, K. J. et al. High-resolution mechanical imaging of glioblastoma by multifrequency magnetic resonance elastography. *PLoS ONE* **9**, e110588 (2014).

40. Safar, M. E. Arterial stiffness as a risk factor for clinical hypertension. *Nat. Rev. Cardiol.* **15**, 97–105 (2018).

41. Engler, A. J., Sen, S., Sweeney, H. L. & Discher, D. E. Matrix elasticity directs stem cell lineage specification. *Cell* **126**, 677–689 (2006).

42. Brauer, E. et al. Collagen fibrils mechanically contribute to tissue contraction in an in vitro wound healing scenario. *Adv. Sci.* **6**, 1801780 (2019).

43. Yalak, G. & Vogel, V. Extracellular phosphorylation and phosphorylated proteins: not just curiosities but physiologically important. *Sci. Signal.* **5**, re7 (2012).

44. Sussman, M. V. & Katchalsky, A. Mechanochemical turbine: a new power cycle. *Science* **167**, 45–47 (1970).

45. Gallant, M. A. et al. Bone cell-independent benefits of raloxifene on the skeleton: a novel mechanism for improving bone material properties. *Bone* **61**, 191–200 (2014).

46. Zhang, K., Feng, Q., Fang, Z., Gu, L. & Bian, L. Structurally dynamic hydrogels for biomedical applications: pursuing a fine balance between macroscopic stability and microscopic dynamics. *Chem. Rev.* **121**, 11149–11193 (2021).

47. Scarlett, J. M., Hu, S. J. & Alonge, K. M. The 'loss' of perineuronal nets in Alzheimer's disease: missing or hiding in plain sight? *Front. Integr. Neurosci.* **16**, 1–16 (2022).

48. Soares Da Costa, D., Reis, R. L. & Pashkuleva, I. Sulfation of glycosaminoglycans and its implications in human health and disorders. *Annu. Rev. Biomed. Eng.* **19**, 1–26 (2017).

49. Lewis, D. et al. Ultrastructural localization of sulfated and unsulfated keratan sulfate in normal and macular corneal dystrophy type I. *Glycobiology* **10**, 305–312 (2000).

50. Saito, T. et al. Sulfation patterns of keratan sulfate in different macular corneal dystrophy immunophenotypes using three different probes. *Br. J. Ophthalmol.* **92**, 1434–1436 (2008).

51. Hatano, S. & Watanabe, H. Regulation of macrophage and dendritic cell function by chondroitin sulfate in innate to antigen-specific adaptive immunity. *Front. Immunol.* **11**, 232 (2020).

52. Reijmers, R. M., Troeberg, L., Lord, M. S. & Petrey, A. C. Editorial: proteoglycans and glycosaminoglycan modification in immune regulation and inflammation. *Front. Immunol.* **11**, 595867 (2020).

53. Syha, R. et al. Short-term exercise-induced changes in hydration state of healthy Achilles tendons can be visualized by effects of off-resonant radiofrequency saturation in a three-dimensional ultrashort echo time MRI sequence applied at 3 Tesla. *J. Magn. Reson. Imaging* **40**, 1400–1407 (2014).

54. Grosse, U. et al. Influence of physical activity on T1 and T2* relaxation times of healthy Achilles tendons at 3T. *J. Magn. Reson. Imaging* **41**, 193–201 (2015).

55. Bohm, S., Mersmann, F. & Arampatzis, A. Human tendon adaptation in response to mechanical loading: a systematic review and meta-analysis of exercise intervention studies on healthy adults. *Sports Med. Open* **1**, 7 (2015).

56. Taylor, W. R. et al. Tibio-femoral joint contact forces in sheep. *J. Biomech.* **39**, 791–798 (2006).

57. Taylor, W. R., Heller, M. O., Bergmann, G. & Duda, G. N. Tibio-femoral loading during human gait and stair climbing. *J. Orthop. Res. Off. Publ. Orthop. Res. Soc.* **22**, 625–632 (2004).

58. Huri, G. et al. A novel repair method for the treatment of acute Achilles tendon rupture with minimally invasive approach using button implant: a biomechanical study. *Foot Ankle Surg.* **19**, 261–266 (2013).

59. Nagelli, C. V. et al. Mechanical and strain behaviour of human Achilles tendon during in vitro testing to failure. *Eur. Cell. Mater.* **43**, 153–161 (2022).

60. Pękala, P. A. et al. The twisted structure of the Achilles tendon unraveled: a detailed quantitative and qualitative anatomical investigation. *Scand. J. Med. Sci. Sports* **27**, 1705–1715 (2017).

61. Labranche, R. et al. Liver iron quantification with MR imaging: a primer for radiologists. *Radiographics* **38**, 392–412 (2018).

62. Spadaro, J. A., Becker, R. O. & Bachman, C. H. The distribution of trace metal ions in bone and tendon. *Calcif. Tissue Res.* **6**, 49–54 (1970).

63. Bellof, G., Most, E. & Pallauf, J. Concentration of copper, iron, manganese and zinc in muscle, fat and bone tissue of lambs of the breed German Merino Landsheep in the course of the growing period and different feeding intensities. *J. Anim. Physiol. Anim. Nutr.* **91**, 100–108 (2007).

64. Nunes, R. et al. Decreased sulfate content and zeta potential distinguish glycosaminoglycans of the extracellular matrix of osteoarthritis cartilage. *Front. Med.* **8**, 612370 (2021).

65. Vining, K. H. et al. Mechanical checkpoint regulates monocyte differentiation in fibrotic niches. *Nat. Mater.* **21**, 939–950 (2022).

66. Agarwal, P. et al. A dysfunctional TRPV4–GSK3β pathway prevents osteoarthritic chondrocytes from sensing changes in extracellular matrix viscoelasticity. *Nat. Biomed. Eng.* **5**, 1472–1484 (2021).

67. Guilak, F., Erickson, G. R. & Ting-Beall, H. P. The effects of osmotic stress on the viscoelastic and physical properties of articular chondrocytes. *Biophys. J.* **82**, 720–727 (2002).

68. Nuri, L., Obst, S., Newsham-West, R. & Barrett, R. Three-dimensional morphology and volume of the free Achilles tendon at rest and under load in people with unilateral mid-portion Achilles tendinopathy. *Exp. Physiol.* **103**, 358–369 (2018).

69. Gillard, G. C., Merrilees, M. J., Bell-Booth, P. G., Reilly, H. C. & Flint, M. H. The proteoglycan content and the axial periodicity of collagen in tendon. *Biochem. J.* **163**, 145–151 (1977).

70. Powder, S. L., Shah, P. H., Potter, H. G. & Koff, M. F. The effect of freeze-thawing on magnetic resonance imaging T2* of freshly harvested bovine patellar tendon. *Quant. Imaging Med. Surg.* **5**, 368–373 (2015).

71. Fishbein, K. W. et al. Effects of formalin fixation and collagen cross-linking on T2 and magnetization transfer in bovine nasal cartilage. *Magn. Reson. Med.* **57**, 1000–1011 (2007).

72. Money, N. P. Osmotic pressure of aqueous polyethylene glycols. *Plant Physiol.* **91**, 1373–1380 (1989).

73. Herrmann, K. H., Gärtner, C., Güllmar, D., Krämer, M. & Reichenbach, J. R. 3D printing of MRI compatible components: why every MRI research group should have a low-budget 3D printer. *Med. Eng. Phys.* **36**, 1373–1380 (2014).

74. Bydder, M., Rahal, A., Fullerton, G. D. & Bydder, G. M. The magic angle effect: a source of artifact, determinant of image contrast, and technique for imaging. *J. Magn. Reson. Imaging* **25**, 290–300 (2007).

75. Herrmann, K. H., Krämer, M. & Reichenbach, J. R. Time efficient 3D radial UTE sampling with fully automatic delay compensation on a clinical 3T MR scanner. *PLoS ONE* **11**, e0150371 (2016).

76. Fram, E. K. et al. Rapid calculation of T1 using variable flip angle gradient refocused imaging. *Magn. Reson. Imaging* **5**, 201–208 (1987).

77. Springer, F., Steidle, G., Martirosian, P., Claussen, C. D. & Schick, F. Effects of in-pulse transverse relaxation in 3D ultrashort echo time sequences: analytical derivation, comparison to numerical simulation and experimental application at 3 T. *J. Magn. Reson.* **206**, 88–96 (2010).

78. Feinberg, D. A. & Oshio, K. Gradient-echo shifting in fast MRI techniques (ERASE imaging) for correction of field inhomogeneity errors and chemical shift. *J. Magn. Reson.* **97**, 177–183 (1992).

79. Krämer, M. et al. Immersion of Achilles tendon in phosphate-buffered saline influences T1 and T2* relaxation times: an ex vivo study. *NMR Biomed.* **33**, e4288 (2020).

80. Zwart, N. R., Johnson, K. O. & Pipe, J. G. Efficient sample density estimation by combining gridding and an optimized kernel. *Magn. Reson. Med.* **67**, 701–710 (2012).

81. Juras, V. et al. Bi-exponential T2* analysis of healthy and diseased Achilles tendons: an in vivo preliminary magnetic resonance study and correlation with clinical score. *Eur. Radiol.* **23**, 2814–2822 (2013).

82. Neeb, H., Ermer, V., Stocker, T. & Shah, N. J. Fast quantitative mapping of absolute water content with full brain coverage. *NeuroImage* **42**, 1094–1109 (2008).

83. Legant, W. R. et al. Measurement of mechanical tractions exerted by cells in three-dimensional matrices. *Nat. Methods* **7**, 969–971 (2010).

84. Vogel, V. & Sheetz, M. Local force and geometry sensing regulate cell functions. *Nat. Rev. Mol. Cell Biol.* **7**, 265–275 (2006).

Author contributions

M.R.K., M.K., N.M.B., P.F., V.V. and G.N.D. conceived the research. M.R.K. developed the experimental set-up and performed and analysed the in vitro experiments, including tissue collection and preparation, mechanical and swelling characterization, histology imaging, and osmolality measurements, and coordinated in vivo scans. M.K. developed the MRI sequences and the experimental MRI set-up, and performed and analysed the MRI scans. S.T. diagnosed and recruited the patients. V.S. and P.F. conducted and analysed the SAXS experiments. M.R.K., M.K and N.M.B. analysed and interpreted the data. S.T., T.H.Q., P.F., V.V., J.R.R. and G.N.D. interpreted the data. M.R.K. wrote the paper. All authors read and contributed to editing the paper.

Competing interests

The authors declare no competing interests.

Additional information

Extended data is available for this paper at https://doi.org/10.1038/s41551-025-01369-w.

Supplementary information The online version contains supplementary material available at https://doi.org/10.1038/s41551-025-01369-w.

Correspondence and requests for materials should be addressed to Georg N. Duda.
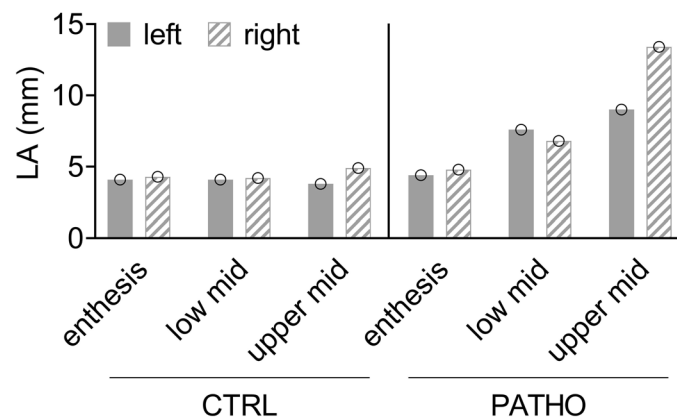
Peer review information *Nature Biomedical Engineering* thanks Jiang Du, Guy Genin, Yin-Yuan Huang and Fritz Schick for their contribution to the peer review of this work. Peer reviewer reports are available.

Reprints and permissions information is available at www.nature.com/reprints.

Publisher's note Springer Nature remains neutral with regard to jurisdictional claims in published maps and institutional affiliations.

Extended Data Fig. 1 | Comparison of tendon thickness along the Achilles tendon computed from in vivo scans between an asymptomatic control subject (CTRL) and a patient (PATHO) with diagnosed mid-portion Achilles tendinopathy. Tendon thickness was quantified by the longest axis in a cross-section (LA). LA was greater for the patient in both the lower (low mid) and upper part (upper mid) of the tendon mid-portion, particularly on their right foot with the diagnosed tendinopathy. Greater tendon thickness on the patient's left foot may have been a result of abnormal loading due to pain avoidance gait. Bar plots show a single value for each region of interest from $n = 1$ Achilles tendons.
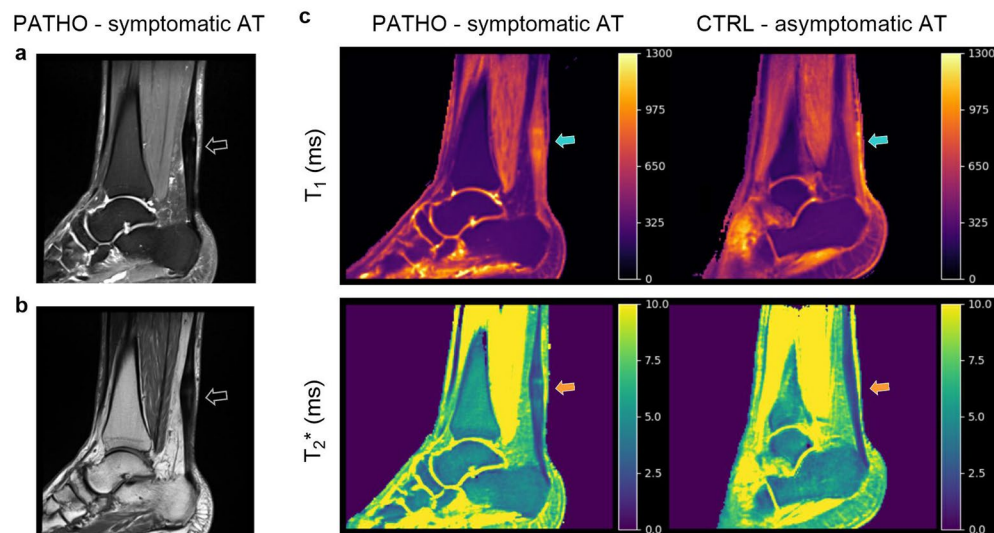
Extended Data Fig. 2 | MRI scans performed in vivo on a patient shows the gained insight into tissue properties by the UTE sequences compared with standard clinical imaging sequences for tendon. A patient (male, 48 years old) with diagnosed mid-portion Achilles tendinopathy was scanned. MR images obtained from scans with standard clinical **a**, PD-weighted and **b**, T_1-weighted sequences for the symptomatic Achilles tendon (PATHO - symptomatic AT). **c**, T_1 and T_2^* maps of the Achilles tendon obtained from MRI scans using UTE sequences for both the symptomatic foot of the patient (PATHO - symptomatic AT) and the asymptomatic contralateral foot of the patient (CTRL - asymptomatic AT).
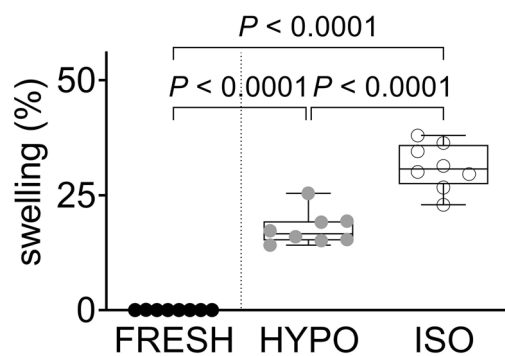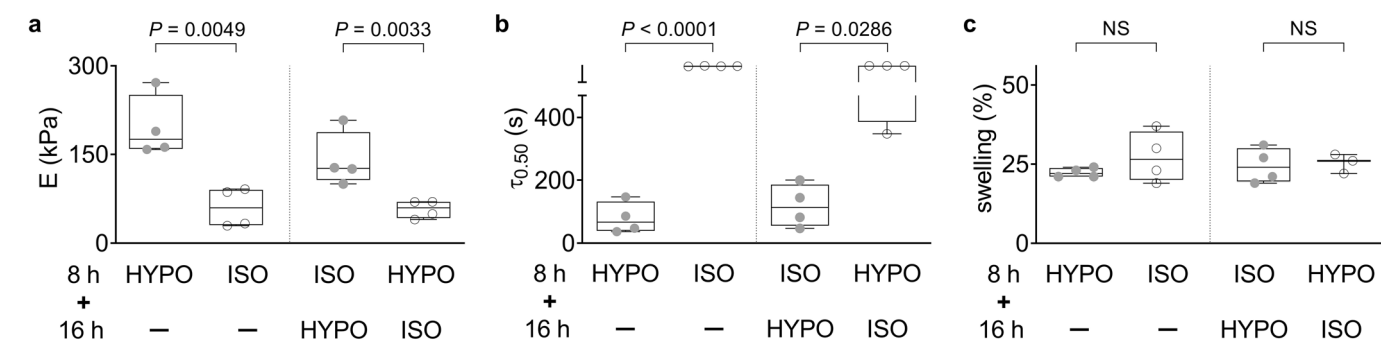
Extended Data Fig. 3 | Swelling after 24 h exposure of ECM samples to HYPO and ISO solutions compared with samples in FRESH condition. Measurements were carried out in parallel with MRI and mechanical characterization. Quantification revealed water uptake of 18 ± 3.6% in HYPO and 31 ± 5.0% in ISO conditions after 24 h. P values were determined using two-tailed t-tests for $n = 8$ biological samples. Box plot information: box limits show 25th and 75th percentiles, box middle lines show medians, and whiskers show minimum and maximum values.
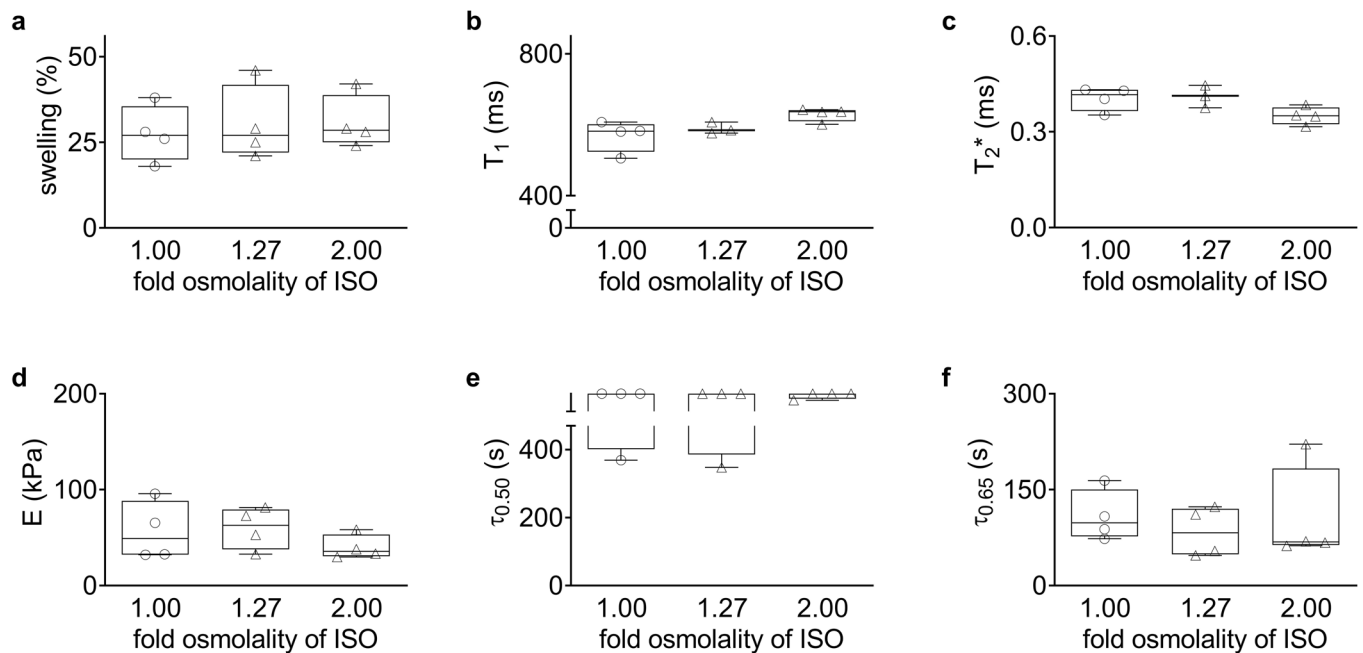
Extended Data Fig. 4 | Hyper-osmolar environments with osmolality increased by higher ion concentration showed a large proportion of more loosely bound water in the ECM, similar to ISO condition. Swelling, water binding, and mechanics were not significantly affected, even by double ISO osmolality. Triangle symbols indicate conditions with increased ion buffer concentration compared with ISO conditions (circles). These results support the design of the ex vivo ECM model and experimental set-up, which used HYPO and ISO conditions as extreme comparisons of low and high proportions of more loosely bound water, respectively. ECM samples were characterized by **a**, swelling, **b**, T_1 values **c**, T_2^* values, **d**, elastic modulus E, and stress relaxation time **e**, $\tau_{0.50}$ and **f**, $\tau_{0.65}$. Statistical analyses were performed in **a, c**, and **d**, using one-way ANOVA with Tukey's multiple comparisons tests, and in **b, e**, and **f**, using Kruskal-Wallis tests with Dunn's multiple comparison tests. The analyses were conducted for $n = 4$ biological samples, except in **c**, which used $n = 3$ biological samples for comparisons involving the condition of 1.27-fold osmolality of ISO. Significance threshold: $P < 0.05$. Box plot information: box limits show 25th and 75th percentiles, box middle lines show medians, and whiskers show minimum and maximum values.

Extended Data Fig. 5 | Exposure of ECM samples to alternating osmolality indicates reversibility of mechanical changes. a, Elastic modulus E, **b**, stress relaxation time $\tau_{0.50}$ and **c**, swelling; left: samples after incubation for 8 h in HYPO or ISO; right: samples initially subjected to swelling in one osmolality (HYPO or ISO) and then exposed to the other osmotic condition for another 16 h. Statistical analyses were performed using two-tailed t-tests, except in **b**, where two-tailed Mann-Withney test was used for the comparison between ISO + HYPO and HYPO + ISO. The analyses were conducted for $n = 4$ biological samples, except in **c**, which used $n = 3$ biological samples for the comparison involving the condition HYPO + ISO. Box plot information: box limits show 25th and 75th percentiles, box middle lines show medians, and whiskers show minimum and maximum values.
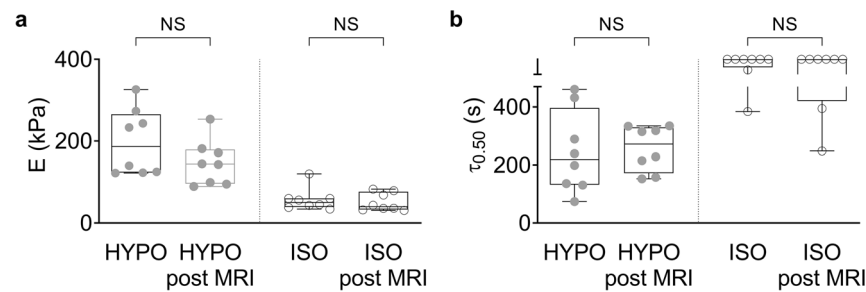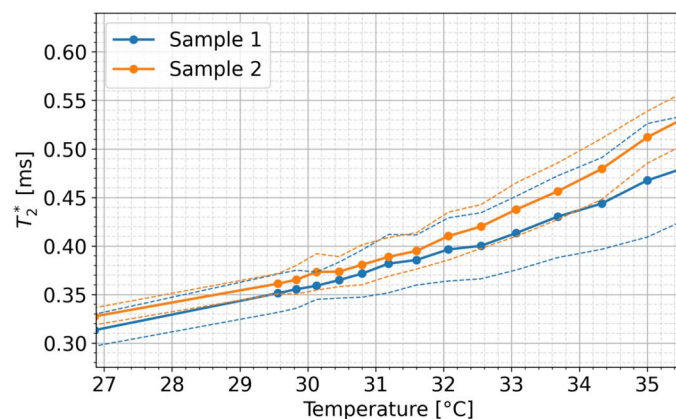
Extended Data Fig. 6 | Mechanical characterization after MRI analysis to verify the reproducibility and stability of ex vivo ECM tuning by changes in the osmotic environment ion concentration. Additional mechanical characterization of the contralateral tendons after MRI scans (post MRI) shows the reproducibility of the experiments, as no significant differences were observed compared with the mechanical characterization of the ipsilateral tendons. This was tested for both HYPO and ISO swelling conditions, and proves the stability of the effect even at day 5 after tissue excision. The 5 days between excision and measurement comprised 3 days of storage at 4 °C and 2 days of incubation with one MRI scan in between. **a**, Elastic modulus E and **b**, stress relaxation half time $\tau_{0.50}$. Statistical analyses were performed for $n = 8$ biological samples using two-tailed t-tests to compare HYPO and HYPO-post MRI conditions, and two-tailed Wilcoxon signed-rank tests to compare ISO and ISO-post MRI conditions. Box plot information: box limits show 25th and 75th percentiles, box middle lines show medians, and whiskers show minimum and maximum values.
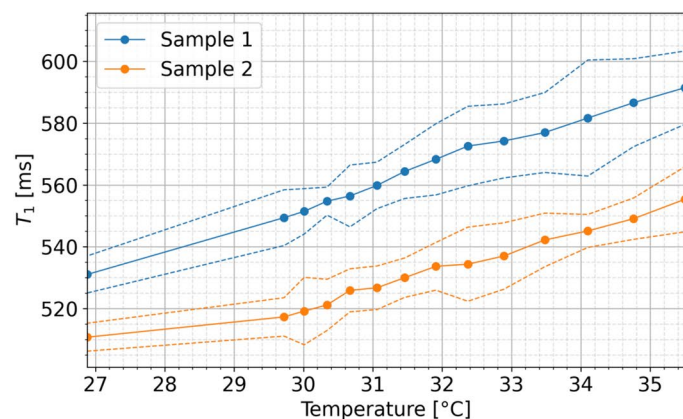
Extended Data Fig. 7 | Temperature-dependence of T_1 and T_2^* relaxation times in ex vivo ovine Achilles tendon. Two fresh ex vivo ovine Achilles tendons were wrapped in a heating pack, and MRI scans were repeated as the temperature inside the heating pack was monitored while cooling down. Both T_1 values (left) and T_2^* values (right) were influenced by the temperature, showing increases at higher temperatures. Notably, the MRI scans of the ex vivo ECM samples in this study were carried out at room temperature to better relate to other characterizations (for example, mechanical, SAXS), which were also performed at room temperature.
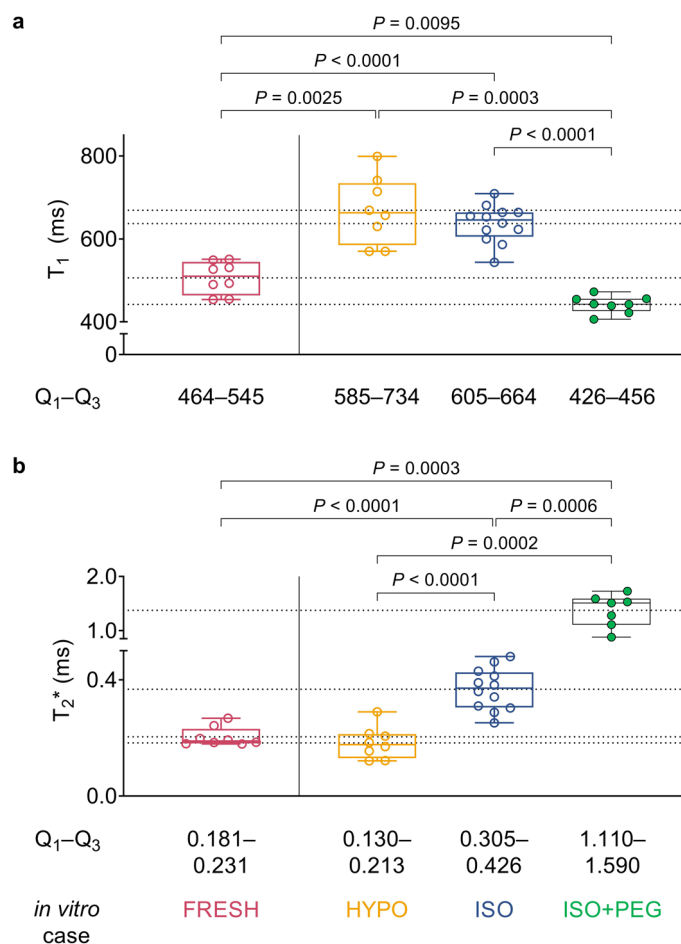
Extended Data Fig. 8 | Overview of MRI T_1 and T_2^* values for the cases presented in the figure summarizing the findings of the study. MRI parameters mapped in FRESH, HYPO, ISO, and ISO-PEG conditions for **a**, T_1 values and **b**, T_2^* values. The ISO + PEG condition shown here includes samples of both 100 kPa and 200 kPa osmotic pressure applied by PEG to ECM samples in ISO solution. Dotted lines indicate the mean value of T_1 or T_2^* in an in vitro case. Value ranges from first to third quartile [Q_1–Q_3] are presented for each condition and MRI parameter. P values were calculated using Brown-Forsythe and Welch ANOVA tests with Dunnett's T3 multiple comparisons tests. Analyses were conducted in **a**, for $n = 8$–12 biological samples, and in **b**, for $n = 7$–12 biological samples. Box plot information: box limits show 25th and 75th percentiles, box middle lines show medians, and whiskers show minimum and maximum values.
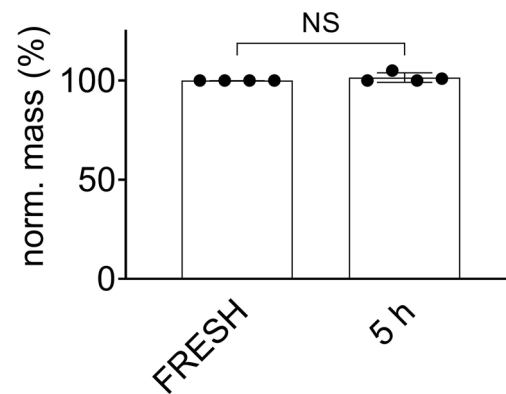
Extended Data Fig. 9 | Testing whether a moist environment in sealed tubes can prevent dehydration of ECM samples for several hours, thereby enabling MRI scans of tendon in the fresh state. Mass of samples held in constant position by a 3D-printed mounting device for 5 h in a sealed 15 ml tube with soaked gauze at the bottom of the tube normalized to the mass in FRESH condition. Four samples dissected from one tendon were tested. Each sample was measured twice: in the FRESH condition and after five hours in a sealed tube (5 h). Bar plots show mean ± s.d. The P value was determined using a two-tailed t-test for $n = 4$ samples; significance threshold: $P < 0.05$; NS, not significant.
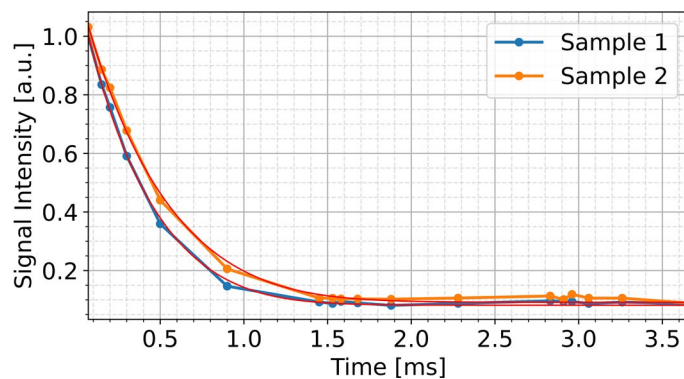
Extended Data Fig. 10 | Signal decay curves in ovine ex vivo Achilles tendon samples in fresh condition. Two Achilles tendons, excised from one animal, were stored under conditions avoiding dehydration, as described in the Methods section, and heated to body temperature (~37 °C, using heat pads) for the scans. Decay curves of two tissue samples are shown by orange and blue solid lines, respectively, connecting the normalized signal intensity measured at different echo times (filled circles). For echo times beyond 1.5 ms, the signal intensity of the samples dropped below 10%, remaining at a level comparable to image noise. Red lines show a mono-exponential fit. The decay curves closely align with a mono-exponential model, with no indication of bi-component signal characteristics. T_2^* of the ex vivo samples was quantified as 0.55 ms.

Corresponding author(s): Georg Duda

Last updated by author(s): Oct 23, 2024

Reporting Summary

Nature Portfolio wishes to improve the reproducibility of the work that we publish. This form provides structure for consistency and transparency in reporting. For further information on Nature Portfolio policies, see our Editorial Policies and the Editorial Policy Checklist.

Statistics

For all statistical analyses, confirm that the following items are present in the figure legend, table legend, main text, or Methods section.

n/a	Confirmed	
☐	☒	The exact sample size (*n*) for each experimental group/condition, given as a discrete number and unit of measurement
☐	☒	A statement on whether measurements were taken from distinct samples or whether the same sample was measured repeatedly
☐	☒	The statistical test(s) used AND whether they are one- or two-sided *Only common tests should be described solely by name; describe more complex techniques in the Methods section.*
☒	☐	A description of all covariates tested
☐	☒	A description of any assumptions or corrections, such as tests of normality and adjustment for multiple comparisons
☐	☒	A full description of the statistical parameters including central tendency (e.g. means) or other basic estimates (e.g. regression coefficient) AND variation (e.g. standard deviation) or associated estimates of uncertainty (e.g. confidence intervals)
☐	☒	For null hypothesis testing, the test statistic (e.g. *F*, *t*, *r*) with confidence intervals, effect sizes, degrees of freedom and *P* value noted *Give P values as exact values whenever suitable.*
☒	☐	For Bayesian analysis, information on the choice of priors and Markov chain Monte Carlo settings
☒	☐	For hierarchical and complex designs, identification of the appropriate level for tests and full reporting of outcomes
☐	☒	Estimates of effect sizes (e.g. Cohen's *d*, Pearson's *r*), indicating how they were calculated

Our web collection on statistics for biologists contains articles on many of the points above.

Software and code

Policy information about availability of computer code

Data collection	No specific software was used for data collection besides the work-system-specific software included in the used MRI scanners (MAGNETOM Vida, software XA20A, Siemens Healthineers; MAGNETOM Prisma, software VE11B and XA30A, Siemens Healthineers; BioSpec USR 94/20, software ParaVision 6.0.1, Bruker) and in the mechanical characterization system (TestBench LM1 system, software WinTest version 7, BOSE).
Data analysis	Mechanical and MRI data were analysed using MATLAB (The MathWorks) versi-n R2019b and Python version 3.9. Images were analysed using the ImageJ version 1.54f. Statistical analyses were performed using GraphPad Prism version 9.5.1.

For manuscripts utilizing custom algorithms or software that are central to the research but not yet described in published literature, software must be made available to editors and reviewers. We strongly encourage code deposition in a community repository (e.g. GitHub). See the Nature Portfolio guidelines for submitting code & software for further information.

Data

Policy information about [availability of data](#)

All manuscripts must include a [data availability statement](#). This statement should provide the following information, where applicable:
- Accession codes, unique identifiers, or web links for publicly available datasets
- A description of any restrictions on data availability
- For clinical datasets or third party data, please ensure that the statement adheres to our [policy](#)

> The main data supporting the results in this study are available within the paper and its Supplementary Information. Source data for the figures are provided with this paper. The raw and analysed datasets generated during the study are available for research purposes from the corresponding author on reasonable request.

Research involving human participants, their data, or biological material

Policy information about studies with [human participants or human data](#). See also policy information about [sex, gender (identity/presentation), and sexual orientation](#) and [race, ethnicity and racism](#).

Reporting on sex and gender	Three human participants were included in the study (two male and one female). The findings were considered irrespective of a participant's sex. Sex was self-reported. No identifiable data were reported. No sex-and-gender-based analyses were performed ,as pathological tissue alterations related to the considered pathology (tendinopathy) were expected to be independent of sex or gender in the context of this study.
Reporting on race, ethnicity, or other socially relevant groupings	Not relevant to the study.
Population characteristics	One healthy asymptomatic control participant (male, 34 years old) without known pathologies, two patients (female, 53 years old; male, 48 years old) with mid-portion Achilles.
Recruitment	Participants were recruited through the involved clinician (Senior Consultant for surgery).
Ethics oversight	Ethics Board of the Charité – Universitätsmedizin Berlin.

Note that full information on the approval of the study protocol must also be provided in the manuscript.

Field-specific reporting

Please select the one below that is the best fit for your research. If you are not sure, read the appropriate sections before making your selection.

☒ Life sciences ☐ Behavioural & social sciences ☐ Ecological, evolutionary & environmental sciences

For a reference copy of the document with all sections, see [nature.com/documents/nr-reporting-summary-flat.pdf](#)

Life sciences study design

All studies must disclose on these points even when the disclosure is negative.

Sample size	The study was performed with 44 fresh Achilles tendons harvested from 22 sheep right after euthanasia (Supplementary Fig. 1). Eight tendons were used for the main part of the study,and multiple tissue probes of a tendon were used per condition tested. With this, high measurement realiability was achieved. Subsequent focus experiments built up on the established setup and main part of the study, and employed a lower number of tendons.
Data exclusions	Tissue samples were placed in a custom-made mounting device to hold a sample in position during incubation and the MRI scans. However, if a sample would have tilted (e.g., during MRI scan preparation), measured MRI $T2^*$ values for the tilted sample would be excluded as $T2^*$ can be affected by altered fibre alignment.
Replication	in vivo human MRI scans (Fig. 1, Supplementary Fig. 3) were performed within a case study of one healthy control participant and two patients. For the main part of the study (Figs. 2–4), MRI, mechanical and swelling measurements were performed on ECM samples dissected from tendons of eight animals; eight ECM samples were used per tendon and experimental condition. Representative tissue-structure images were produced with histological stainings and high resolution MRI on ECM samples of two animals of the set. Extending the main part of the study, detailed aspects were investigated (Figs. 5,6) using the established experimental setup and ECM samples from three to four tendons.
Randomization	For the study, ex vivo tissue of adult sheep was used to ensure comparable tissue-property conditions. From each Achilles tendon mid-portion, multiple tissue probes were dissected and assigned randomly to different incubation conditions.
Blinding	Blinding was not required for the performed study on ex vivo tissue probes. Measurements were performed using measurement systems that provide objective and discrete values. Tissue preparation and measurements were carried out according to defined protocols. Analysis was performed using standardized software protocols to achieve objective and discrete read-outs, irrespective of the user of the software.

Reporting for specific materials, systems and methods

We require information from authors about some types of materials, experimental systems and methods used in many studies. Here, indicate whether each material, system or method listed is relevant to your study. If you are not sure if a list item applies to your research, read the appropriate section before selecting a response.

Materials & experimental systems

n/a	Involved in the study
☒	Antibodies
☒	Eukaryotic cell lines
☒	Palaeontology and archaeology
☐ ☒	Animals and other organisms
☒	Clinical data
☒	Dual use research of concern
☒	Plants

Methods

n/a	Involved in the study
☒	ChIP-seq
☒	Flow cytometry
☒	MRI-based neuroimaging

Animals and other research organisms

Policy information about studies involving animals; ARRIVE guidelines recommended for reporting animal research, and Sex and Gender in Research

Laboratory animals	For the ex vivo analyses, tissue samples were harvested from animals after euthanasia. To keep the number of animals to a minimum, the samples were taken from other research projects but with no relationship that would affect the tissue properties of the samples (G0424/17, G0210/18).
Wild animals	The study did not involve wild animals.
Reporting on sex	The sex of the animals was not considered to be relevant to the purpose of this study, as only physiological tissue of animals, without relevant pathology, was collected.
Field-collected samples	The study did not involve samples collected from the field.
Ethics oversight	In compliance with the ethical guidelines of legal, local animal rights protection authorities (Landesamt für Gesundheit und Soziales Berlin).

Note that full information on the approval of the study protocol must also be provided in the manuscript.